Expanding the ice inventory of NGC 1333 IRAS 2A with INDRA using JWST observations: tracing organic refractories and beyond

Rayalacheruvu, P.; Majumdar, L.; Monteiro Rocha, W.R.; Ressler, M.E.; Giri, P.R.; Maitrey, S.; ... ; Klaassen, P.D.

The Astrophysical Journal Supplement Series, 281:51 (35pp), 2025 December https://doi.org/10.3847/1538-4365/ae112f

Expanding the Ice Inventory of NGC 1333 IRAS 2A with INDRA Using JWST Observations: Tracing Organic Refractories and Beyond

Prathap Rayalacheruvu[1,2], Liton Majumdar[1,2], W. R. M. Rocha[3], Michael E. Ressler[4], Pabitra Ranjan Giri[1,2], S. Maitrey[1,2], Karen Willacy[4], D. C. Lis[4], Yuan Chen[3], and P. D. Klaassen[5]
[1] Exoplanets and Planetary Formation Group, School of Earth and Planetary Sciences, National Institute of Science Education and Research, Jatni 752050, Odisha, India; liton@niser.ac.in, dr.liton.majumdar@gmail.com
[2] Homi Bhabha National Institute, Training School Complex, Anushaktinagar, Mumbai 400094, India
[3] Leiden Observatory, Leiden University, PO Box 9513, NL 2300 RA Leiden, The Netherlands
[4] Jet Propulsion Laboratory, California Institute of Technology, 4800 Oak Grove Drive, Pasadena, CA 91109, USA
[5] UK Astronomy Technology Centre, Royal Observatory Edinburgh, Blackford Hill, Edinburgh EH9 3HJ, UK
Received 2025 June 16; revised 2025 September 14; accepted 2025 September 16; published 2025 December 1

Abstract

In the era of the James Webb Space Telescope (JWST), with its unprecedented sensitivity and spectral resolution, infrared spectral surveys have revealed a rich inventory of ices, including complex organic molecules (COMs), in young stellar objects. However, robust methods to decompose and quantify these absorption features, particularly across broad spectral ranges, are still under investigation. We present the Ice-fitting with NNLS-based Decomposition and Retrieval Algorithm (INDRA), a fully Python-based tool that performs continuum and silicate removal, global ice fitting using weighted nonnegative least-squares (NNLS), and estimates column densities and statistical significance. We apply INDRA to NGC 1333 IRAS 2A, a target from the JWST Observations of Young protoStars (JOYS+) program previously studied using local fitting. We derive optical depths via polynomial continuum subtraction and remove silicate absorption using a synthetic model, isolating ice features for global MIRI fitting. Our results are consistent with previous local fits, confirming simple species and COMs, and expand the inventory by identifying additional absorption features from CO_2 and NH_4^+. We also propose the presence of organic refractories contributing up to 9.6% in the spectral region of ∼5–8 μm among the various ice components, whose inclusion significantly improves the global spectral fitting. These broad absorption features, extending across ∼5.5–11 μm, are likely produced by large, complex molecules containing carbonyl (C=O), hydroxyl (O–H), amine (N–H), and C–H bending modes. Our expanded inventory, now incorporating these organic residues, offers new insights into the chemical evolution of ices in star-forming regions and highlights the importance of global spectral fitting in constraining ice compositions.

Unified Astronomy Thesaurus concepts: Protostars (1302); Star formation (1569); Astrochemistry (75); James Webb Space Telescope (2291)

1. Introduction

Molecules form in dense molecular clouds, where low temperatures allow gas-phase species to freeze onto dust grains and also promote chemical reactions on grain surfaces, leading to the formation of icy mantles. These ices are predominantly composed of water (H_2O), carbon monoxide (CO), methane (CH_4), and other simple molecules, which later end up in planet-forming disks where future planets and other planetary bodies form (K. I. Öberg & E. A. Bergin 2021). Understanding the ice chemistry in young stellar objects (YSOs), an intermediate stage in planet formation, provides a unique window into the evolving conditions from cold molecular clouds to planet-forming disks. The icy mantles not only serve as reservoirs for simple molecules but also play a critical role in the formation of complex organic molecules (COMs). Examining the composition and column densities of ices in YSOs provides valuable insights into the physical and chemical conditions in which these ices form and evolve during star and planet formation (A. C. A. Boogert et al. 2015).

Gas-phase observations have revealed the chemical diversity of both low-mass and high-mass YSOs (e.g., J. K. Jørgensen et al. 2020). While gas-phase COMs are well characterized through millimeter observations, the identification of solid-phase COMs remained challenging prior to the launch of the James Webb Space Telescope (JWST), due to limited spectral resolution and overlapping features in infrared (IR) absorption spectra. Methanol (CH_3OH) is the only securely detected COM in interstellar ices, identified via IR absorption spectroscopy using facilities such as the United Kingdom Infrared Telescope, Infrared Space Observatory (ISO), Very Large Telescope, AKARI, and Spitzer (R. J. A. Grim et al. 1991; C. J. Skinner et al. 1992; E. Dartois et al. 1999; E. Dartois et al. 2003; E. L. Gibb et al. 2004; K. M. Pontoppidan et al. 2004; W. F. Thi et al. 2006; A. C. A. Boogert et al. 2008; S. Bottinelli et al. 2010; T. Shimonishi et al. 2010; L. E. U. Chu et al. 2020). Other COMs, such as ethanol (CH_3CH_2OH) and acetaldehyde (CH_3CHO), have been tentatively identified based on Spitzer and ground-based data, but their detections remain ambiguous due to spectral blending and the absence of distinct spectral features (W. A. Schutte et al. 1999; K. I. Öberg et al. 2011; J. Terwisscha van Scheltinga et al. 2018).

JWST is revolutionizing our understanding of chemical diversity of star-forming regions by offering unprecedented

sensitivity and resolution across the IR spectrum. One of its key instruments, the Mid-Infrared Instrument (MIRI; G. H. Rieke et al. 2015, G. S. Wright et al. 2015, G. S. Wright et al. 2023), operates in four modes, including the Medium-Resolution Spectroscopy (MRS; M. Wells et al. 2015, A. Labiano et al. 2021, I. Argyriou et al. 2023). JWST's MIRI-MRS offers a significant improvement in spectral resolution ($R \sim$ 1300–3700) over the Spitzer Infrared Spectrograph (IRS; $R \sim$ 60–600), enabling the identification of individual ice absorption bands that were previously blended. This is particularly crucial for studying COMs in the MIRI wavelength range (A. Labiano et al. 2021; Y.-L. Yang et al. 2022; Y. Chen et al. 2024; W. R. M. Rocha et al. 2024), helping to trace the transport of COMs from the early stages of star formation to later evolutionary phases. Additionally, JWST's full spectral coverage and high sensitivity enable simultaneous measurements of CO and CO_2 ices, including their isotopologues, facilitating a more comprehensive analysis using carbon isotopic ratios to further constrain evolutionary processes (N. G. C. Brunken et al. 2024). These capabilities provide new opportunities to study the chemical evolution of interstellar ices and their role in the formation of larger COMs during various stages of star and planet formation. In this context, the JWST guaranteed time observation time (GTO) program JWST Observations of Young protoStars (JOYS) aims to characterize the physical and chemical processes occurring in both high-mass and low-mass star-forming regions using near- and mid-infrared spectra of molecules in both the gas and ice phases. Early results from the JOYS program reveal a rich chemical diversity of species in both the gas and ice phases across several sources (Y. Chen et al. 2024; W. R. M. Rocha et al. 2024; M. L. van Gelder et al. 2024).

Studying the formation and evolution of COMs holds significant importance in star and planet formation studies and remains an active area of research. Studies like S. Manigand et al. (2020), A. Belloche et al. (2020), M. L. van Gelder et al. (2020), J. K. Jørgensen et al. (2020), P. Nazari et al. (2021), and C. Gieser et al. (2021), etc., have elaborated on the formation of COMs. They primarily form on the surfaces of interstellar dust grains during the cold early stages when $T \sim 10$ K, leading to the development of ice mantles. Simple species like CO can undergo hydrogenation and radical recombination in the ice mantle, initiating the formation of COM precursors. The presence of energetic processes such as UV irradiation and cosmic rays further drives the COM chemistry, leading to the formation of even larger COMs. UV photoprocessing and thermal processing both play important roles in the evolution of COM chemistry. For example, the ion CH_3^+, observed in the gas phase, is commonly associated with UV-driven reactions. In the solid phase, species like OCN^- can form through acid–base reactions, which are efficiently mediated by both thermal processing and UV photoprocessing of HNCO-containing ices. These chemical pathways, triggered by energetic photons and charged particles, contribute to the buildup of organic refractory residues, including compounds of potential astrobiological significance. Laboratory experiments by T. Javelle et al. (2024) showed that irradiation and thermal alteration of simple ices like CH_3OH, H_2O, and NH_3 can produce diverse organic molecules that include residual organic compounds containing up to 78 carbon atoms, 188 hydrogen atoms, and 37 oxygen atoms. R. G. Urso et al. (2024) carried out similar experiments involving simple ices and found the destruction of pristine frozen compounds and the formation of new species that survived until 300 K. These refractory organics potentially become part of dust grains in planet-forming regions and later agglomerate into comets and asteroids. As a result, some of the organic matter present in the solar system may have been inherited from the earliest stages of its formation. G. Danger et al. (2024) have demonstrated how this matter can evolve inside asteroids, parent bodies of meteorites, in our solar system using an analytical approach. The residues inherited may undergo further processing depending on the local conditions. For example, studies by J. Mathurin et al. (2024) and R. Carrasco-Herrera et al. (2024) have shown how these materials are altered inside asteroids like Ryugu and the Jovian moon Europa, respectively. However, in environments with milder processing conditions, such as comets, these materials are more likely to remain unaltered, preserving a record of the early chemistry of the solar system, and offer crucial insights into the origin and evolution of COMs. Studying the chemical inventory of both low-mass and high-mass protostellar environments enhances our understanding of how organic refractories form and survive before becoming incorporated into planetary bodies.

The low-mass Class 0 protostar NGC 1333 IRAS 2A (hereafter IRAS 2A), located in the Perseus molecular cloud ($\sim$299 pc), is a well-known hot corino with a rich inventory of gas-phase COMs (S. Bottinelli et al. 2007). Gas-phase glycolaldehyde ($HCOCH_2OH$), a key prebiotic molecule, has been detected in this source (A. Coutens et al. 2015; V. Taquet et al. 2015; M. De Simone et al. 2017). M. L. van Gelder et al. (2024) recently confirmed the mid-infrared emission of SO_2 in IRAS 2A for the first time. Based on the rotational temperature, the spatial extent of SO_2 emission, and the narrow line widths in Atacama Large Millimeter/submillimeter Array data, they suggested that SO_2 likely originates from ice sublimation in the central hot core around the protostar, rather than from an accretion shock. Furthermore, IRAS 2A hosts a protobinary system with collimated jets, whose shocks and associated energetic processing are expected to significantly influence ice chemistry (G. Sandell et al. 1994; L. W. Looney et al. 2000; B. Reipurth et al. 2002; J. J. Tobin et al. 2015). While gas-phase studies of IRAS 2A have yielded substantial insights, solid-phase studies have been limited due to the low spectral resolution of earlier facilities and the inherently blended nature of ice absorption features. However, observations with JWST have now revealed rich ice absorption signatures with high signal-to-noise ratios (S/Ns), enabling more detailed analysis. W. R. M. Rocha et al. (2024) studied IRAS 2A in the ice-COM fingerprint region between 6.8 and 8.6 μm, estimating the column densities of various complex organic and simple ices. Their findings shed light on how these ices may be formed, evolve, and be inherited by icy cometary bodies. They also reported a good correlation between the ice abundances observed in comet 67P and those in IRAS 2A. The detected ices in IRAS 2A include CH_3CHO and larger organics with multiple carbon atoms such as CH_3OCH_3 and C_2H_5OH, as well as ions like $HCOO^-$ and OCN^-. Y. Chen et al. (2024) also examined another low-mass protostar, B1-c, and found similar ice components as that of IRAS 2A. Their gas-to-ice comparisons of COMs in both sources revealed that molecules such as CH_3OCH_3 and CH_3OCHO show similar abundance ratios in both phases, while CH_3CHO and C_2H_5OH

are more abundant in the ice phase. This suggests that inheritance-driven processes play a significant role, alongside possible gas-phase reprocessing. These findings highlight the complex interplay between ice chemistry, gas-phase reactions, and physical processes in shaping the chemical evolution of COMs in star-forming regions. While these studies have offered valuable insights into the chemistry of IRAS 2A, they were typically limited to specific spectral regions, particularly within the 6.8–8.8 μm range. This region, however, lies within a broader absorption feature spanning 5–11 μm, whose origin remains uncertain. Although H_2O has a bending mode at around 5.8 μm, it cannot contribute entirely to the observed absorption dip across this interval. In order to account for the 5–8 μm absorption region, A. C. A. Boogert et al. (2008) have analytically constructed a spectrum, defined as C5, by subtracting known features from linear combinations of observed spectra, making it an analytical diagnostic component. Though the nature of the C5 component is not fully explored, they related it to the flat profile of the high-temperature H_2O ice bending mode, the overlap of other negative ions (HCO_3^-, NO_3^-, NO_2^-), or organic refractory residue. We note that the absorption in the 5–8 μm region is likely due to a combination of all these factors, but to what extent remains unclear. Studies of other protostellar sources suggest that processed ices, including refractory organic residues formed by energetic processing, may contribute significantly to the absorption near 6 μm. For instance, W33 A shows the deepest 6 μm excess absorption, attributed by E. L. Gibb & D. C. B. Whittet (2002) to a refractory organic component produced by UV processing of icy mantles. Similar components are evident in AFGL 7009S, Mon R2 IRS 3, and NGC 7538 IRS 9, where subtraction of the dominant H_2O feature leaves residuals well explained by such organic material. The use of organic refractory spectra obtained through experimental measurements can help us understand the extent to which refractories shape the C5 component of A. C. A. Boogert et al. (2008) in the 5–8 μm absorption region. Furthermore, the absorption bands of H_2O and CO_2 longward of 10 μm in the observed spectrum of the source have yet to be thoroughly characterized. Utilizing the full MIRI spectral range ($\sim$5–28 μm) allows for a more comprehensive characterization of these absorption bands, thereby providing critical insights into the physical and chemical environment of IRAS 2A, including potential signatures of energetic processing. Moreover, this extended coverage is especially important in the COM region, where features can be spectrally blended with signatures from refractory organic residues that are byproducts of energetic processing of COM ices. Access to the full MIRI range enables a clearer distinction between pristine and processed ices, offering a more complete picture of the chemical evolution occurring in the protostar.

This work focuses on quantifying the ice inventory of IRAS 2A across the full MIRI wavelength range, offering crucial insights into the chemical evolution of protostellar ices. To achieve this, we developed the Ice-fitting with NNLS-based Decomposition and Retrieval Algorithm (`INDRA`), a Python-based tool designed to perform spectral decomposition of ice absorption features using laboratory ice spectra. The structure of the paper is as follows. Section 2 provides an overview of the observations of IRAS 2A. Section 3 describes the ice-fitting tool `INDRA`, detailing the methods used for continuum removal, silicate absorption feature subtraction, and the ice-fitting technique. In Section 4, we present the global fitting results for the IRAS 2A protostar over the complete MIRI range and compare the derived ice column densities with those obtained by W. R. M. Rocha et al. (2024) using a local fitting approach. The discussion is provided in Section 5, and our conclusions are outlined in Section 6.

2. Observations

NGC 1333 IRAS 2A (RA $03^h28^m55\overset{s}{.}57$, decl. $+31^d14^m36\overset{s}{.}97$) was observed using the JWST as part of the GTO program 1236 (P.I. M. E. Ressler). The observations were carried out with MIRI-MRS. The target was observed using a single pointing in two-point dither mode, with dedicated background observations in the same mode. All three gratings (A, B, and C) were employed, providing full wavelength coverage from 4.9 to 28 μm. The FASTR1 readout mode was utilized, and the integration time for each grating was 111 s. The data were processed through the three stages of the JWST calibration pipeline (H. Bushouse et al. 2022), using the reference context `jwst_0994.pmap` of the Calibration Reference Data System (P. Greenfield & T. Miller 2016). The raw `uncal` data were initially reduced with the `Detector1Pipeline`, followed by the `Spec2Pipeline`. In this stage, fringe corrections were applied using the extended source fringe flat, supplemented by a residual fringe correction. The telescope background was subtracted using the dedicated background observation. Subsequently, the `Spec3Pipeline` was used to produce data cubes for all 12 subbands, with both the master background and outlier rejection routines switched off.

The observations revealed continuum emission associated only with the primary component of the IRAS 2A binary system. The spectrum was extracted from the continuum peak at 5.5 μm, located at R.A. (J2000) $03^h28^m55\overset{s}{.}57$ and decl. (J2000) $+31^d14^m36\overset{s}{.}76$. The aperture diameter was set to $4 \times 1.22\lambda/D$ to maximize the captured source flux while minimizing noise. The estimated 1σ rms noise increases from approximately 0.4 mJy at wavelengths below 15 μm to a few mJy at 19 μm and exceeds 10 mJy for wavelengths longer than 22 μm. The spectrum shows a typical profile of an embedded protostar and shows absorption features attributed to various ice molecules. Broad H_2O absorption bands are visible at 5.5–8 μm (bending mode) and 10–20 μm (libration mode). In addition, strong silicate absorption features appear near 9.8 and 18 μm. Narrow emission lines present in the spectrum have been masked in this work, as the focus is on ice absorption features. The IRAS 2A spectrum was binned by a factor of 4 across the 8–12 μm wavelength range to improve the S/N as this region is saturated with silicate emissions.

3. Methodology

In this section, we provide details about the ice-fitting tool `INDRA`, which is designed for global continuum removal, silicate feature elimination, ice absorption fitting using laboratory data, and estimation of ice column densities. The tool also includes functionality for applying a Savitzky–Golay (Savgol) filter (A. Savitzky & M. J. E. Golay 1964; J. Luo et al. 2005) to smooth selected laboratory data, along with robust statistical analysis tools to assess the quality of the fit. The various components of the tool are outlined in Figure 1.

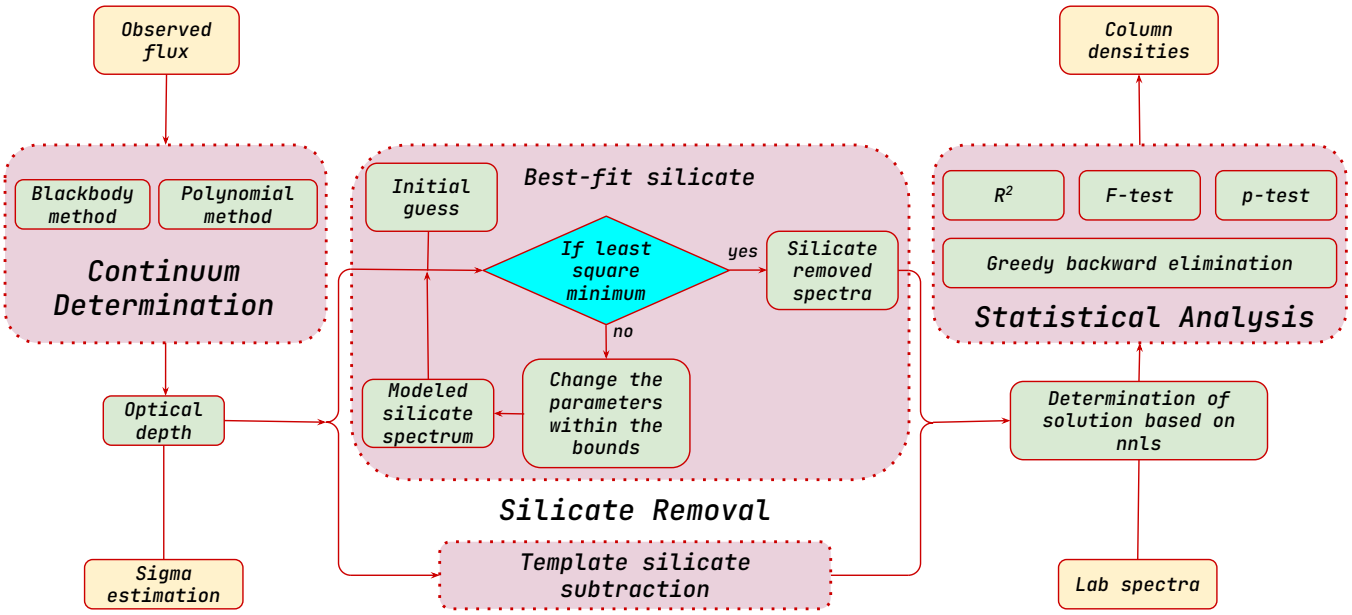

Figure 1. Schematic representation of the methodology for deriving the ice column densities using INDRA. The process includes continuum determination, followed by silicate feature removal and global ice fitting using NNLS. Statistical analysis is performed to assess fit quality and uncertainties after which final column densities are estimated.

3.1. Continuum Removal

In order to constrain the ice absorption features and estimate accurate column densities, it is imperative to determine the continuum and remove it from the observed data before fitting for laboratory ices. However, accurately identifying the continuum spectral energy distribution (SED) poses several challenges, particularly in the wavelength range from 5 to 30 μm, where ice absorption features not only overlap with silicate features but also blend with other ice absorption bands. Additionally, the absorption bands can show a wide range of widths and shapes depending upon the local chemical inventory, further complicating the continuum determination. W. R. M. Rocha et al. (2021) have detailed some of the challenges in determining the continuum in this wavelength range. The continuum SED shortward of 5 μm can be better constrained because of the lack of ice absorption features except for some narrow features of CO_2 and CO ices that appear at around 4.27 and 4.67 μm, respectively. Several methods for constraining the continuum SED at these wavelengths have been documented in the literature. For example, continuum estimation using Kurucz stellar atmosphere models for wavelengths below 4 μm (K. M. Pontoppidan et al. 2004), and a linear combination of blackbodies to fit the near- and mid-infrared (IR) wavelengths (M. Ishii et al. 2002), can not only estimate the continuum SED, but also constrain physical properties such as extinction and effective temperature.

In this study, we adopt the two continuum estimation methods between 5 and 30 μm proposed by W. R. M. Rocha et al. (2021):

(1) A polynomial approach, where a low-order polynomial given by Equation (1) is used to estimate the continuum:

$$F_{\rm poly}(\lambda) = \sum_{k=0}^{n} a_k \lambda^k. \quad (1)$$

Here, n is the order of the polynomial, λ is the wavelength, and a_k are the polynomial coefficients that determine the contribution of each power of wavelength to the overall continuum shape.

(2) A multitemperature blackbody approach, where the continuum is modeled as a sum of blackbody curves, as described by Equation (2):

$$F_{\rm BB}(\lambda, T) = \sum_{i=1}^{m} f_i \frac{2hc^2}{\lambda^5} \left(\frac{1}{\exp\left(\frac{hc}{\lambda k_{\rm B} T_i}\right) - 1} \right). \quad (2)$$

Here, T_i is the temperature of the ith blackbody, λ is the wavelength, $k_{\rm B}$ is Boltzmann's constant, c is the speed of light, h is Planck's constant, and f_i is a scaling factor.

To achieve continuum subtraction, the INDRA tool enables users to interactively select guiding points for polynomial continuum fitting. The tool then identifies the continuum based on these user-defined points and calculates the continuum SED. These guiding points serve as anchors for optical depth calculations. Once selected, the tool fits the continuum using a user-defined polynomial of finite order. It then calculates the optical depth using Equation (3), thereby consolidating the absorption features in optical depth scale:

$$\tau(\lambda) = -\ln\left(\frac{F_{\rm obs}(\lambda)}{F_{\rm cont}(\lambda)}\right). \quad (3)$$

3.2. Silicate Feature Removal

To isolate ice absorption features in the mid-infrared spectra, we remove the silicate contributions by modeling their synthetic optical depth, followed by baseline correction methods. This is necessary to address the overlapping silicate absorption bands around 9.8 and 18 μm with key ice features. Previous studies of protostars employed a silicate profile observed toward the Galactic center source (GCS 3) as a template (A. C. A. Boogert et al. 1997, S. Bottinelli et al. 2007). However silicate profiles can come in different shapes

Table 1
Silicate Grain Parameters

Parameter	Typical Values
Core composition	Pyroxene, carbon, etc.
Core mass fraction	Pyroxene (0.82), carbon (0.18)
Surface density	$\sim 10^5$ g cm^{-2}
Mantle composition	H_2O
Mantle fraction	0–0.5
Grain geometry	DHS, CDE
Porosity	0.8

Note. DHS: distribution of hollow spheres; CDE: continuous distribution of ellipsoids. These grain geometries are used to model irregular silicate grain shapes.

and sizes, and using GCS 3 as a template silicate may not completely remove the silicate features. Instead, it can introduce spurious features as demonstrated in Figures A.1 and A.2 of W. R. M. Rocha et al. (2024). To overcome this limitation, the INDRA tool offers two approaches to removing silicate features: one utilizing a predefined silicate model and another modeling the synthetic silicate spectra by exploring the silicate composition parameter space. Both approaches are discussed below.

3.2.1. Template Silicate Subtraction

In this approach, we use a predefined silicate absorption model derived from observational or laboratory data, or an educated guess. The known silicate components are scaled to match the observed spectrum, ensuring that their contribution is accurately subtracted. This approach is particularly useful when the silicate composition is well constrained, allowing for a straightforward removal of the silicate absorption without requiring extensive modeling. However, it requires a precise knowledge of the surface densities and compositions of different silicate components, and their mass fractions, which is not always possible.

3.2.2. Synthetic Silicate Model

In the second approach, we explore the parameter space consisting of different silicate components with varying surface densities and mass fractions. We utilize the optool code (C. Dominik et al. 2021) to generate the optical depth spectra of the silicates. The silicate parameters that can be modeled using INDRA are shown in Table 1.

To determine the synthetic silicate model, we simultaneously fit both the 9.8 and 18 μm bands. Once the synthetic silicate optical depths of different components are computed, a baseline correction is applied to each spectrum to remove any continuum variations or underlying broad features that could interfere with the fitting process. Following the baseline correction, the spectra are recombined using scaling factors applied to each silicate species to best match the observed data, and in particular to match the 9.8 and 18 μm absorption features. In this process, we optimize the scaling factors, the mass fractions of silicates, and their surface densities using a nonlinear least squares fitting procedure as shown in Figure 1 and thereby determine the best fit for the silicate absorption profiles.

We note that the placement of the continuum is closely tied to the silicate absorption, particularly at wavelengths longer than 7.4 μm. In this region, the continuum shape is primarily dictated by the depth and extent of the silicate profile—higher continuum placement corresponds to stronger inferred silicate absorption. Consequently, using appropriate silicate models allows for the effective removal of their contribution, helping to isolate the underlying ice absorption features. At shorter wavelengths ($\lesssim$7.4 μm), the observed spectrum contains relatively featureless regions (e.g., 4.8–5.6 μm), which provide more reliable anchors for continuum placement. Nevertheless, the continuum shape over the silicate region should still be considered to ensure consistency across the entire spectrum. We note that significant uncertainties remain in both the continuum placement and the silicate modeling. A more rigorous treatment of these uncertainties would require detailed radiative transfer modeling, which is beyond the scope of the present comparative study. As demonstrated in previous works (e.g., W. R. M. Rocha et al. 2024, 2025), such detailed modeling is not essential for ice studies like this. In practice, a variety of approaches have been used to estimate and remove the silicate absorption. In some cases, a polynomial continuum is first fitted to the spectrum, followed by the application of a simple silicate absorption model (W. R. M. Rocha et al. 2024) or a multispline function (W. R. M. Rocha et al. 2025) to isolate the ice features. More sophisticated modeling is needed to simultaneously account for both the continuum and the silicate features in a physically consistent manner. However, our primary objective in this work is not to model the continuum and silicate features in detail, but rather to assess the robustness of ice column density estimates using a global continuum approach and to expand the chemical inventory of IRAS 2A leveraging the full MIRI spectra of the source.

3.3. Laboratory Ice Data

The laboratory ice data used in INDRA consist of 772 ice spectra, provided in the format of wavenumber versus absorbance. The data are compiled from publicly available ice databases such as the Leiden Ice Database,[6] the NASA Cosmic Ice Laboratory,[7] UNIVAP[8], and the Optical Constant Database[9] that have comprehensive spectroscopic measurements of ices relevant to astrophysical environments. Some key ices include CO, H_2O, CH_4, NH_3, and organic molecules that have been observed in various astrophysical environments including low-mass star-forming regions. The spectra are measured in the laboratory under various physical conditions representing those of star-forming regions, providing us a wide range of data useful for ice fitting of YSOs. Before using the laboratory data in INDRA, we conducted a survey of the ices that are potentially contributing to the observed optical depths. This is because the spectra of the same ice components are recorded at different temperatures. Though the band profiles are temperature dependent, most absorption features remain largely unaffected, posing a risk of overfitting if all the components are included. To mitigate this, we selected 76 components for the final fitting, the details of which are found in Appendix A. These spectra are essential for accurately fitting the observed ice absorption features. To ensure proper

[6] https://icedb.strw.leidenuniv.nl
[7] https://science.gsfc.nasa.gov/691/cosmicice/spectra.html
[8] https://www1.univap.br/gaa/nkabs-database/data.htm
[9] https://ocdb.smce.nasa.gov/

fitting, the spectra are preprocessed, which involves applying baseline corrections to select ice components to enhance the clarity of absorption features or to isolate minor component features that might otherwise be obscured by stronger ones. For this work, we correct the baselines of specific ice components, particularly those involving organic molecules in water mixtures where H_2O features dominate (see Appendix C). Once compiled, the data can be used in INDRA fitting, where we further normalize the laboratory spectra to facilitate comparison with observational data.

3.4. Ice Fitting Using Weighted NNLS

This study employs a weighted nonnegative least-squares (weighted-NNLS) algorithm to fit laboratory ice absorption spectra to the observed spectra of the YSO. The weighted-NNLS method ensures that all fitted coefficients remain nonnegative, which is physically meaningful for the absorption spectra and ensures that the fitted components remain above the sigma noise estimate. The laboratory ice absorption spectra consist of several ices each with a distinct absorption profile. The observed spectrum can be modeled as a linear combination of these profiles scaled by appropriate nonnegative coefficients. The weighted-NNLS method is applied to determine these scaling factors and thereby determine the contribution of each such ice to the absorption spectra. The following is a description of the algorithm.

Let the observed spectrum be represented as a vector $\mathbf{y} \in \mathbb{R}^n$ with each element y_i corresponding to the observed flux at wavelength λ_i. Similarly let $\boldsymbol{A} \in \mathbb{R}^{n\times m}$ represent the matrix of laboratory ice absorption spectra where each column $\boldsymbol{A}_j$ is the absorption profile of a specific ice component. The objective of the fitting process is to find the nonnegative coefficient vector $\boldsymbol{x} \in \mathbb{R}^m$ where each element x_j represents the scaling factor of the corresponding ice component such that the residual between the observed and modeled spectrum is minimum.

The weighted-NNLS problem can be formulated as

$$\min_{\boldsymbol{x}} \sum_{i=1}^{n} w_i^2 \left(y_i - \sum_{j=1}^{m} A_{ij} x_j \right)^2. \tag{4}$$

Here, w_i is the weight given by $\frac{1}{\sigma_i}$, where σ_i is the observational uncertainty at wavelength λ_i. The weighting ensures that data points with larger uncertainties have a smaller contribution to the total residual.

The NNLS algorithm solves for the minimization criteria given by Equation (4) subject to the constraint that $x_j \geqslant 0$ for all j. This ensures that the fit does not include any unphysical negative contributions from any of the ice components.

Convergence is reached when the residual cannot be reduced further while maintaining the nonnegativity constraint on the coefficients. By using the weighted-NNLS method, we ensure that the laboratory ice absorption profiles are optimally scaled to match the observed spectrum, providing robust estimates of the ice column densities in the observed source.

3.5. Estimation of Statistical Significance

Accurate noise estimation is crucial in spectroscopic analysis, particularly when identifying weak absorption features in the optical depth spectrum and ascertaining the accuracy of the spectral fitting. A common approach, which has also been used by W. R. M. Rocha et al. (2024), is to assume a fixed 10% noise level across the spectrum. While this assumption may be reasonable for high-S/N spectra with uniform noise at all wavelengths, it does not account for variations in baseline fluctuations, instrumental response, or wavelength-dependent noise. Consequently, such a fixed uncertainty can lead to either an overestimation or underestimation of the actual noise, potentially affecting the reliability of spectral fits. To obtain a more accurate estimate of the noise, we employ a polynomial-based approach similar to that of Y. Chen et al. (2024). Instead of assuming a fixed percentage, the noise level is estimated at multiple spectral regions devoid of strong absorption features, and an average value is taken across these regions. Appropriate polynomials are used to model and subtract the baseline fluctuations, ensuring that the noise estimation reflects the true uncertainties in the data. The noise level at each region is calculated using

$$\sigma = \sqrt{\frac{\sum_{i=1}^{N}(y_i - \bar{y})^2}{N}} \tag{5}$$

where y_i represents the polynomial-subtracted optical depth at each spectral channel within the selected region, and $\bar{y}$ is the mean value of y_i. This method provides a robust uncertainty estimate, crucial for assessing the significance of weak absorption features and the reliability of the fits. By averaging over multiple regions, it captures the global noise characteristics across the wavelength range rather than relying on a single estimate. The computed noise level is then incorporated into our statistical analysis to ensure a reliable interpretation of the spectral fits.

3.5.1. Greedy Backward Elimination as a Check against Overfitting

As a check against overfitting, we use the greedy backward elimination approach based on a chi-square statistical evaluation using the Equation (6):

$$\chi^2 = \sum_i \frac{(O_i - E_i)^2}{\sigma_i^2}, \tag{6}$$

with O_i representing the observed data points, E_i the model values for those data points, and σ_i the estimated uncertainty given by Equation (5). This method iteratively removes each component from the model while preserving the rest and evaluates the χ^2 value to assess the goodness-of-fit. At each step, we systematically remove one component at a time and fit the rest of the components using weighted-NNLS. The component whose removal results in the smallest increase in χ^2 is identified as the least significant and is tentatively eliminated. To ensure whether a specific component meaningfully contributes to the fit, we compute the p-value. This test is based on the null hypothesis that the component in question does not contribute significantly to the model, meaning any change in the fit quality upon removing the component is purely due to random fluctuations rather than a true effect. To test this, we compare the fit quality before and after the component is removed, using the difference in χ^2 values ($\Delta\chi^2 = \chi^2_{\text{before}} - \chi^2_{\text{after}}$). Under the null hypothesis, the test statistic follows a chi-square distribution with degree of freedom, ν, equal to the number of omitted components. The p-value is then computed from the cumulative distribution

function of the χ^2 distribution:

$$p = 1 - F_{\chi^2}(\Delta\chi^2, \nu) \tag{7}$$

where the function $F_{\chi^2}(\Delta\chi^2, \nu)$ represents the cumulative probability of observing a chi-square value up to $\Delta\chi^2$ under the null hypothesis. A high p-value ($p > 0.05$) suggests that the difference in chi-square is small and likely due to random fluctuations rather than a meaningful improvement in fit. In this case, the removed component is deemed statistically insignificant, justifying its elimination. Conversely, if the p-value falls below a predefined threshold ($p \leqslant 0.05$), the change in chi-square is large enough to indicate that the removed component significantly contributes to the model, and it should be retained. By evaluating the statistical significance of component removal using p-values, we ensure that only the most relevant components are retained in the fit, thereby preventing overfitting while maintaining an optimal representation of the observed data.

3.5.2. R^2 Statistic to Assess the Goodness-of-fit

The goodness-of-fit is assessed using the coefficient of determination (R^2), which quantifies how well the model explains the variance in the observed data as each component is being added. It is given by

$$R^2 = 1 - \frac{\sum_{i=1}^{n}(y_i - \hat{y}_i)^2}{\sum_{i=1}^{n}(y_i - \bar{y})^2} \tag{8}$$

where y_i are the observed values, $\hat{y}_i$ are the model-predicted values, and $\bar{y}$ is the mean of the observed data. An R^2 value close to 1 indicates that the model explains most of the variance in the data, while a value near 0 suggests poor explanatory power. While calculating the R^2 statistic as each component is added, we consider only its contributing region, defined as the wavelength range where the component's contribution exceeds the sigma level calculated for the source.

3.5.3. F-Statistic to Evaluate the Relevance of Minor Components

We note that, while greedy backward elimination (GBE) helps identify components that are important for the overall model, it does not provide a quantitative measure of statistical significance, especially for minor components. To address this, we performed an F-test, which evaluates whether adding a specific component significantly improves the model fit or not and to what extent. The F-value for each component is computed using Equation (9).

$$F = \frac{\left(\frac{\mathrm{RSS_{test}} - \mathrm{RSS_{full}}}{\mathrm{df_{test}} - \mathrm{df_{full}}}\right)}{\left(\frac{\mathrm{RSS_{full}}}{N - \mathrm{df_{full}}}\right)} \tag{9}$$

where $\mathrm{RSS_{full}}$ is the residual sum of squares (RSS) for the full model (including the tested component), $\mathrm{RSS_{test}}$ is the RSS for the reduced model (excluding the tested component), $\mathrm{df_{full}}$ and $\mathrm{df_{test}}$ are the degrees of freedom of the full and reduced models, respectively, and N is the total number of data points. The F-values are computed as the ratio of the variance explained by each component to the residual variance and indicate the relative contribution of each component to the overall fit. In this sense, it offers an additional check along with GBE, which uses χ^2 statistic. Note that we use only the relevant wavelength window of each component specific to its contribution to the fitting while evaluating F-value. A higher value indicates that the tested component significantly improves the fit by reducing the residual variance in that wavelength window. Empirical thresholds for spectral fitting applications suggest the following classification of F-values:

1. strong contribution: $F > 10$
2. moderate contribution: $2 < F < 10$
3. weak contribution: $F < 2$.

We note that these ranges are not strictly defined, and their interpretation depends on the sample size, degrees of freedom, etc.

The statistical significance of each component is further evaluated using the corresponding p-value, which represents the probability of obtaining an F-statistic as extreme as observed under the null hypothesis. This time the p-value is computed as

$$p = P(F > F_{\mathrm{obs}}) \tag{10}$$

where F_{obs} is the observed F-statistic. A lower p-value (typically $p < 0.05$) suggests that the inclusion of the component significantly improves the model.

3.5.4. Estimation of Confidence Intervals

To quantify uncertainties in the best-fit coefficients for the ice absorption modeling and to estimate confidence intervals in the column densities, we generate perturbed coefficients by sampling values linearly spaced around each best-fit coefficient. Specifically, for each coefficient C_i, perturbed values were sampled uniformly between $C_i - \epsilon C_i$ and $C_i + \epsilon C_i$, where ϵ is a fractional error factor defining the perturbation range.

For each perturbed coefficient set, a synthetic spectrum y_{model} is generated, and its fit to the observed optical depth spectrum y_{obs} is evaluated using the normalized chi-square statistic given by

$$\chi^2_{\mathrm{norm}} = \frac{\sum\left(\frac{y_{\mathrm{obs}} - y_{\mathrm{model}}}{\sigma_y}\right)^2}{\sum y^2_{\mathrm{model}}}, \tag{11}$$

where σ_y is the observational uncertainty.

Confidence intervals are then determined for each coefficient by identifying the range of C_i values corresponding to an acceptable increase in χ^2_{norm}. The lower and upper bounds in the coefficients are then used to calculate the minimum and maximum optical depths, setting limits on the column densities for each ice, computed as described in Section 3.6.

The correlations between different ice components vary with wavelength due to the presence of complex mixtures, which can induce shifts in absorption band positions and alter band shapes. As a result, uncertainties and parameter correlations are not uniform across the spectral range, and a global analysis may not effectively capture these localized effects. Therefore, we perform the analysis in a sliding-window, local manner across the spectrum to account for wavelength-dependent uncertainties. This localized approach enables robust estimation of coefficient significance, their

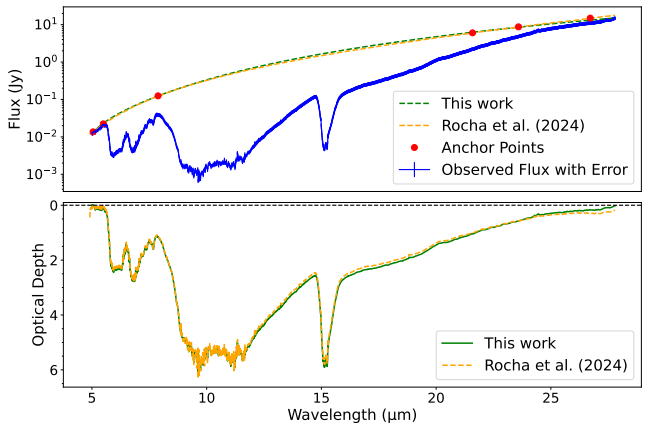

Figure 2. Continuum determination in the source IRAS 2A. The top panel displays the observed flux (blue) on a logarithmic scale, along with the continuum (green) traced using a guided polynomial fit. The anchor points used for continuum fitting are marked as red dots. The bottom panel presents the corresponding estimated optical depths (green). For comparison, data from W. R. M. Rocha et al. (2024) are also plotted (orange).

correlations, and the associated error bars in the derived column densities.

For each coefficient, the overall lower bound is taken as the minimum of all lower bounds obtained from individual sliding windows, while the overall upper bound is taken as the maximum of all upper bounds from these windows. This method ensures a comprehensive estimation of the confidence intervals.

3.6. Column Density Estimation

Once the best-fit solution is found, we calculate the column density of each ice using Equation (12),

$$N_{\rm ice} = \frac{1}{A}\int_{\nu_1}^{\nu_2} \tau_{\rm lab}(\nu)d\nu \qquad (12)$$

where A represents the vibrational mode band strength of the molecule. The band strengths vary with the chemical environment, making their accurate determination crucial for reliable column density estimates. While calculating the column densities, we incorporate corrected band strength values from the literature. Appendix B provides the list of all the band strengths used in this work. It is to be noted that derivation of band strengths is inherently dependent on ice density, leading to typical uncertainties of approximately 15% for pure ices and 30% for mixed ices (M. G. Rachid et al. 2022; K. Slavicinska et al. 2023).

4. Results

In this section we present the fitting results for IRAS 2A across the entire MIRI wavelength range (5–28 μm). This includes the continuum removal, silicate subtraction, global ice fitting, statistical analysis, and the final estimation of ice column densities. Additionally, we compare our results with previous study that employed a local fitting approach.

4.1. Continuum Determination in IRAS 2A

The continuum fit and the corresponding optical depths of the source IRAS 2A are presented in Figure 2. The continuum and the optical depths calculated by W. R. M. Rocha et al. (2024) are also presented for a comparison. The SED of IRAS 2A is characteristic of embedded protostars, both high-mass and low-mass, exhibiting an increasing slope toward longer wavelengths (E. L. Gibb et al. 2004; A. C. A. Boogert et al. 2008). The observed SED can be modeled using a blackbody approach, assuming contributions from warm dust at wavelengths shorter than 20 μm and cold envelope material at longer wavelengths. However, in this work, a third-order guided polynomial is used to determine the continuum.

This choice is motivated by several factors: (1) the lack of reliable constraints on the temperature components required for blackbody modeling, (2) the flexibility of the polynomial approach in tracing complex absorption features across MIRI, and (3) to maintain consistency with the continuum shape adopted in W. R. M. Rocha et al. (2024), enabling a direct comparison of the resulting ice column densities and evaluation of how different fitting methods influence the derived ice column densities. We use anchor points to trace the continuum, and the same are shown in Figure 2. Please note that some points were placed slightly above the observed data to better approximate the continuum used in the earlier study. However, we emphasize that significant uncertainties are inherently associated with the choice of the continuum, as silicate absorption can extend to longer wavelengths making it challenging to trace it accurately. A detailed treatment of this continuum ambiguity is beyond the scope of the present work. Once the continuum is traced, we convert the spectra into optical depth units using Equation (3).

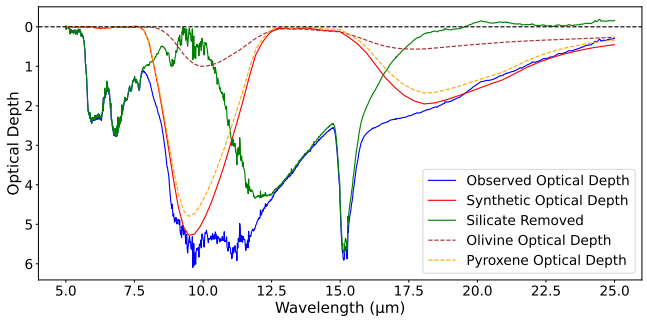

Figure 3. Silicate removal in the source IRAS 2A. The observed optical depth spectrum is shown in blue, while the modeled silicate absorption is represented by the solid red line. The individual silicate components contributing to the overall absorption are olivine (dotted brown) and pyroxene (dotted orange). The final silicate-subtracted spectrum is shown in green.

4.2. Silicate Feature Removal in IRAS 2A

The spectrum of IRAS 2A in optical depth units is shown in the bottom panel of Figure 2. Broad silicate absorption features appear near 9.8 μm, where they partially overlap with organic ice bands, and near 18 μm, where they overlap with H_2O and CO_2 absorption features. In particular, organic ice absorption features embedded within the 9.8 μm region become more distinct once the silicate features and local continuum are removed (W. R. M. Rocha et al. 2024). Additionally, the true shape of the CO_2 band at $\sim$15 μm emerges more clearly after accounting for the overlapping silicate feature near 18 μm. The silicate removed spectra of IRAS 2A are shown in Figure 3. For this work, we adopt a template silicate subtraction method, leveraging the well-constrained silicate model from W. R. M. Rocha et al. (2024) to ensure consistency and accuracy in isolating the ice absorption features. Briefly, the

template silicate model consists of two components: amorphous pyroxene ($Mg_{0.5}Fe_{0.5}SiO_3$) and olivine ($MgFeSiO_4$). Each of these components is assumed to be mixed with carbon, a common constituent of interstellar grains. The volume fractions of silicate and carbon are set to 82% and 18%, respectively. This approach is in line with various protostellar and diffuse interstellar medium models, where carbon fractions can vary between 15% and 30% (J. C. Weingartner & B. T. Draine 2001; K. M. Pontoppidan et al. 2005; P. Woitke et al. 2016). The grain size distribution is modeled using a power-law size distribution with an exponent of 3.5, and grain sizes ranging from 0.1 to 1 μm, consistent with interstellar grain models. To account for the irregular geometry of the dust grains, we adopt a distribution of hollow spheres, a method that provides more realistic fits to the silicate absorption features than simple spherical grain models.

4.3. INDRA Global Fitting Results

The MIRI spectrum of IRAS 2A shows a high S/N and distinct absorption features spanning 5–28 μm. At shorter wavelengths $\lesssim$(10 μm), the spectrum is primarily shaped by absorption from H_2O, organic molecules and organic refractory materials, and silicates. At longer wavelengths ($\gtrsim$10 μm), strong absorptions from H_2O, CO_2, and silicates dominate the spectrum. By subtracting the silicate contributions, the remaining absorption features between 5 and 20 μm can be primarily attributed to ices. The fitting results for the entire MIRI wavelength range of the source IRAS 2A is shown in Figure 4. Our spectral fitting analysis reveals the presence of multiple ice components including simple species such as H_2O, CO_2, and CH_4, as well as COMs like CH_3OH, CH_3CH_2OH, etc. W. R. M. Rocha et al. (2024) carried out local fitting in the COMs fingerprint region (6.8–8.6 μm) of the source and estimated the column densities of COMs present in that region along with H_2O. In this work, we analyze the entire MIRI spectrum and decompose it using a laboratory ice database containing 76 ices, out of which 15 contribute to the global minimum solution. Each of these 15 components shows a peak optical depth that exceeds the noise level in the observed spectrum, indicating appreciable contributions. Their statistical significances are evaluated in Section 4.4.

4.3.1. Absorption Bands of Simple Ices H_2O, CO_2, NH_3, and SO_2

The MIRI spectra of IRAS 2A show broad absorption features of H_2O due to the bending mode at around 6 μm and the libration mode at around 13 μm. The 6 μm region is particularly complex due to significant overlap with absorption features from COMs and other simple molecules. Similarly, the 13 μm region coincides with strong absorption from silicates and CO_2, resulting in blended features that require a combination of pure and mixed ice components for spectral decomposition. The top-right panel in Figure 5 shows the H_2O and CO_2 related best-fit components. All these components are dominant in nature and contribute much to the shape of the overall spectra. H_2O ice appears in both pure and mixed forms, contributing to the bending mode at $\sim$6 μm and the libration mode at $\sim$13 μm. We apply grain-shape correction to the 160 K pure H_2O ice using Mie theory and assuming small grains where it shows a blue wing excess in the 13 μm libration band.

Similarly, the MIRI spectrum of IRAS 2A has a distinct absorption at 15 μm due to CO_2. CO_2 ice appears both in its pure form and as part of mixed ice components. The following components are used to fit the spectrum: pure CO_2 ice, 40 K ice mixture CO:CO_2 in 2:1 ratio, and 10 K ice mixture H_2O:CO_2 in 1:0.14 ratio. Similar ice components were used by K. M. Pontoppidan et al. (2008) and W. R. M. Rocha et al. (2025). The observed double peak in the 15 μm band is likely a result of ice distillation or segregation due to thermal processing and is well fit by pure CO_2 ice. This component shows a prominent blue wing, contributing to the shortward side of the 15 μm band, whereas the 10 K H_2O:CO_2 ice mixture contributes to the red wing of this band. Both K. M. Pontoppidan et al. (2008) and W. R. M. Rocha et al. (2025) found CO_2 ice in H_2O ice-rich environments, which is also the case in the present work. Additionally, contributions from CO ice dominated regions play a role.

Sulfur dioxide (SO_2) shows strong absorption features in the mid-infrared (MIR) region, particularly near 7.7 and 8.5 μm, which correspond to its asymmetric (ν_3) and symmetric (ν_1) stretching modes, respectively. We isolated both these bands of SO_2 from a mixture SO_2:CH_3OH as shown in Figure 15. Ammonia (NH_3) is also found in the fits. The absorption band at 8.9 μm in the observed optical depth spectrum can be related to this ice. Two ice components as shown in Table 2 carry this band in the fits with the H_2O:H_2S–based mixture showing significant contribution to the 8.9 μm band. Notably, this region also overlaps with some minor bands from CH_3CH_2OH, CH_3OH, CH_3CHO, and SO_2, which can lead to blending and a complex shape to the optical depth spectrum. The deviation between the model and the observations in this region may be due to uncertainties in the organic refractory baseline, the placement of the global continuum, the silicate subtraction, or a combination of these factors.

4.3.2. Absorption Bands of NH_4^+, OCN^-, and $HCOO^-$ Ion Salts

Table 3 lists all the ice components that show the spectral features of ions. In our global fitting results, we found the ammonium ion (NH_4^+) in three distinct ice components: within the NH_3:HNCO ice residue that is responsible for the OCN^- ion, in the H_2O:NH_3:CH_3OH:CO:CO_2 ice residue that is responsible for the organic residue shown in Figure 12, and the H_2O:NH_3:H_2S (10:2:1) ice mixture at 135 K. The 6.7 μm band of these ice components can be assigned to the ν_4 mode of NH_4^+ (E. L. Wagner & D. F. Hornig 1950). The broad absorption dip centered around 6.6 μm in the observed optical depth spectrum of IRAS 2A is well explained by these three components, and the model provides an excellent agreement with the data in this region.

Of all the components, the cynate ion (OCN^-) contributes to several bands in the 5–10 μm region and to the $\sim$15 μm band. The spectrum of this ion salt was obtained by J. H. Novozamsky et al. (2001) using an 80 K ice mixture of NH_3:HNCO in 1:1 ratio. The spectral evolution of the mixture when it is gradually being warmed reveals features at approximately 6.67, 7.72, 8.26, and 15.87 μm, which are not associated with the original species. As the temperature increases, these bands grow in intensity while the characteristic bands of HNCO and NH_3 diminish, indicating proton transfer between HNCO and NH_3. The band at 6.67 μm corresponds to the vibrational mode of NH_4^+, whereas the features at 7.72, 8.26, and 15.87 μm are assigned to OCN^-.

Another ion identified in our fitting is the formate ion ($HCOO^-$), which contributes to the bands at 6.32, 7.24, and

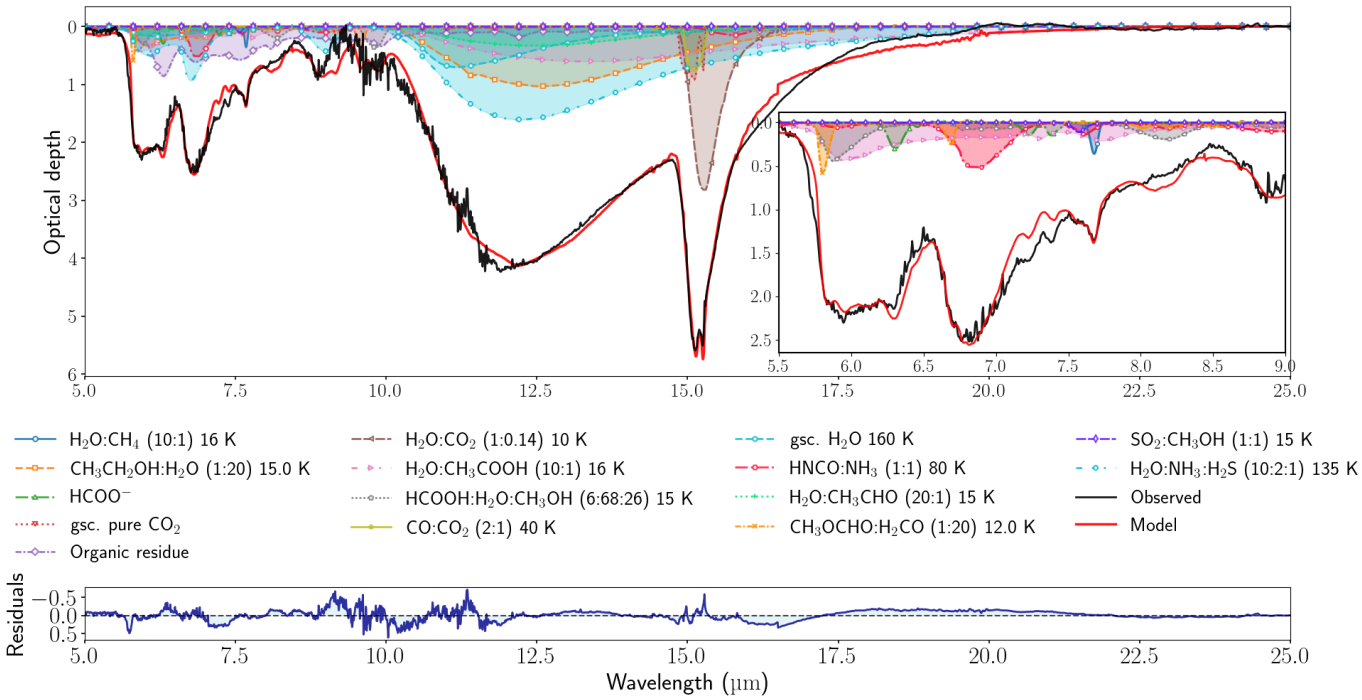

Figure 4. Global ice-fitting results across the entire MIRI spectrum (5–25 μm). The top panel shows the observed optical depth spectrum (solid black) alongside the modeled optical depth spectrum (solid red), which represents the contribution from 15 best-fit ice components. Each contributing component is displayed using different colors, markers, and line styles and are mentioned in the middle panel as a legend. The zoomed-in version of the contribution from select components (weak components) are shown in the inset plot. The bottom panel presents the residuals corresponding to the fit. Note that organic residue refers to the residue spectra obtained by irradiating H_2O:NH_3:CH_3OH:CO:CO_2 ice that shows broad features corresponding to various functional groups, including carbonyl (−C=O), carboxylate ($-COO^-$), amine (–NH_2), and –CN containing species along with hexamethylenetetramine (HMT) and polyoxymethylene (POM). Abbreviations: gsc. = grain-shape corrected.

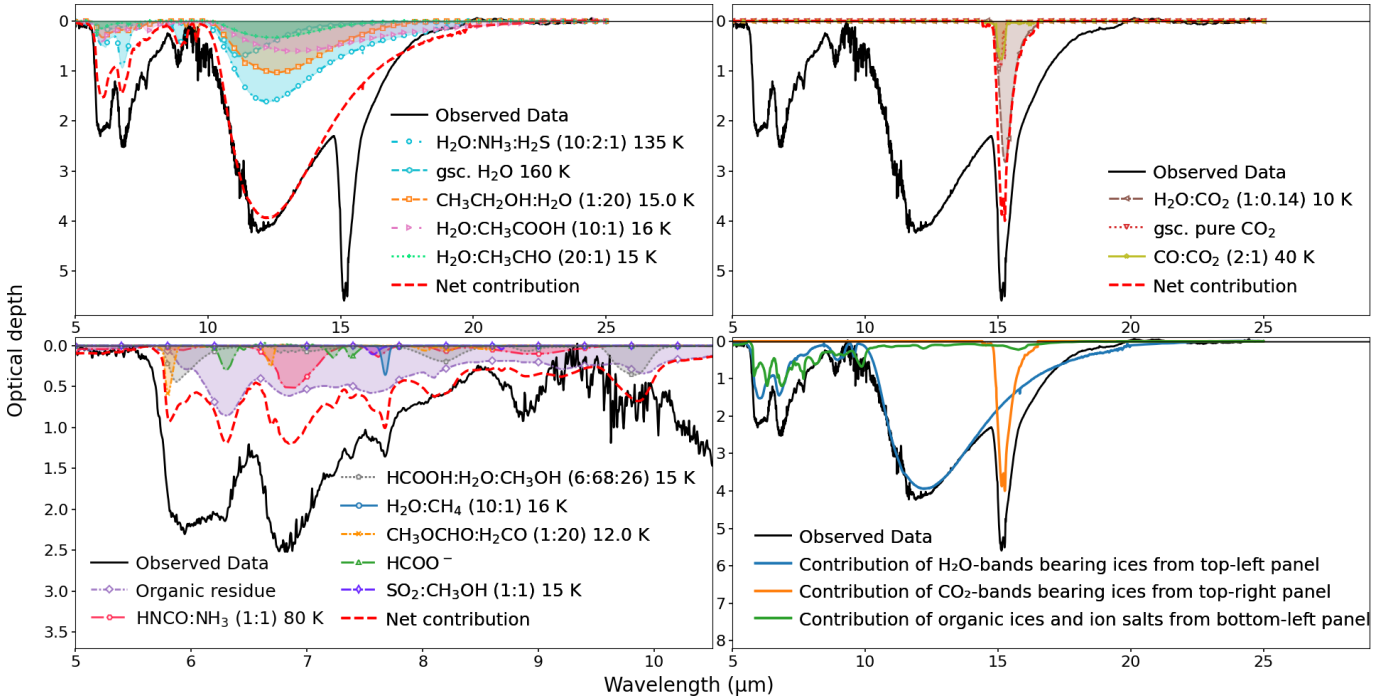

Figure 5. Best-fit decomposition of the MIRI spectrum of IRAS 2A, highlighting the contributions from different ice components. The observed optical depth spectrum is shown in solid black across all panels. Each contributing component is displayed using different colors, markers, and line styles. Top-left panel: contributions from ice components bearing dominant H_2O bands. These components have absorption features spanning from 5–20 μm. Their cumulative contribution to the observed spectrum is shown in dashed red. Top-right panel: contributions from ices bearing CO_2 bands. These components have absorption features spanning from 14–17 μm. Their cumulative contribution to the observed spectrum is shown in dashed red. Bottom-left panel: contributions from ice components that include organic ice mixtures, ions, and organic residue. These components have significant absorption features spanning from 5–11 μm. Their combined contribution to the overall spectrum is shown in dashed red. Bottom-right panel: a summary panel showing the individual contributions (shown in solid colors) to the observed spectrum from the three categories: H_2O band–bearing ices, CO_2 band–bearing ices, and organic ice mixtures along with ions and organic residue.

Table 2
Ice Mixtures Containing H_2O, CO_2, and SO_2

Ice Mixture	Ratio	T (K)
H_2O components	⋯	⋯
H_2O:NH_3:H_2S	10:2:1	135
CH_3CH_2OH:H_2O	1:20	15
H_2O:CH_3COOH	10:1	16
H_2O:CH_3CHO	20:1	15
Pure gsc. H_2O	⋯	160
CO_2 components	⋯	⋯
H_2O:CO_2	1:0.14	10
CO:CO_2	2:1	40
Pure gsc. CO_2	⋯	⋯
SO_2 component	⋯	⋯
SO_2:CH_3OH	1:1	10
NH_3 component	⋯	⋯
H_2O:NH_3:H_2S	10:2:1	135
NH_3:HNCO[a]	1:1	80

Notes. gsc. denotes a grain-shape-corrected component.
[a] Denotes the spectrum of the residual component. For references, see Appendix A.

Table 3
Ice Mixtures Containing Ion Salts

Ice Mixture	Ratio	T (K)	Species
H_2O:NH_3:H_2S	10:2:1	135	H_2O,NH_4^+, NH_3
NH_3:HNCO[a]	1:1	80	OCN^-,NH_4^+, NH_3
H_2O:NH_3:CH_3OH:CO:CO_2[a]	⋯	⋯	NH_4^+
H_2O:NH_3:HCOOH[a]	100:2.6:2	14	$HCOO^-$

Note.
[a] Denotes spectra of the residual components. (For references, see Appendix A.)

7.40 μm. This result is consistent with the findings of W. R. M. Rocha et al. (2024). The spectrum is obtained using the hyperquenching technique on NH_4COOH salts obtained via acid–base reactions involving the 14 K ice mixture of H_2O:NH_3:HCOOH in a ratio 100:2.6:2 (O. Gálvez et al. 2010). To analyze the $HCOO^-$, we isolated its ice bands using a local baseline subtraction method. $HCOO^-$ exhibits a strong band at 6.32 μm, which blends with the intense H_2O absorption at 6 μm, contributing to the excess in this region. Additionally, its 7.2 μm band overlaps with contributions from HCOOH. Therefore, the 7.4 μm band is used to estimate $HCOO^-$ column densities.

4.3.3. Absorption Bands of Organic Molecules

Table 4 summarizes the organic ice components appearing in the fitting. Components where the H_2O bands are retained as mentioned in Table 4 are shown in the top-left panel of Figure 5, and the mixtures where H_2O bands are removed (refer to Appendix C) are shown in the bottom-left panel of the figure to aid visual inspection. All the organic molecules with secure and tentative detections as reported in W. R. M. Rocha et al. (2024) are found in this work.

Table 4
Organic Ice Mixtures Appearing in the Fitting

Ice Mixture	Ratio	T (K)	H_2O Bands
H_2O:CH_4	10:1	16	Removed
HCOOH:H_2O:CH_3OH	6:68:26	15	Removed
CH_3OCHO:H_2CO	1:20	12	⋯
CH_3CH_2OH:H_2O	1:20	15	Retained
H_2O:CH_3COOH	10:1	16	Retained
H_2O:CH_3CHO	20:1	15	Retained

Note. See Section 5.2 and Appendix C for more on H_2O band removal. (References in Appendix A.)

In our analysis, the observed absorption excess at 7.7 μm is attributed to methane (CH_4), which is present in the fits as an H_2O:CH_4 ice mixture. CH_4 has a band at ∼7.7 μm as shown in Figure 13. Due to the interaction with H_2O, CH_4 shows band broadening, leading to a better match with observations when this mixture is considered alongside the OCN^-, SO_2, and CH_3COOH ice bands in the region. An absorption excess in the blue wing of the band is primarily due to OCN^- and SO_2, whereas CH_3COOH contributes to the red wing of the band as shown in the inset plot in Figure 4.

In our fits, formic acid (HCOOH) appears as an HCOOH:H_2O:CH_3OH ice mixture that contributes to several absorption features across the MIRI range, including distinct bands at 5.83 μm (ν_S(C=O)), 6.06 μm (ν_S(C=O)), 7.21 μm (ν_B(OH) and ν_B(CH)), 8.26 μm (ν_S(C–O)), 9.32 μm (ν_B(CH)), 10.75 μm (ν_B(OH)), and 14.18 μm (ν_B(OCO)). Additionally, HCOOH's interaction with H_2O results in a feature at 5.88 μm. Blending effects arise due to the presence of other species in the mixture. Methanol (CH_3OH) shows absorption bands at 6.85, 8.85, and 9.75 μm, overlapping with HCOOH features and contributing to the complexity of the spectrum. The band at 9.74 μm is due to the C–O stretch and fits well within the observed spectrum. This band falls in a region where the absorption band is saturated and a factor multiplication of 2 is applied to the column density estimations, which is also aligned with W. R. M. Rocha et al. (2024). The deviation between the model and the observed optical depth spectrum around the 8.26 μm region may be due to the uncertainties in the refractory material baseline, the placement of the global continuum, or any combination of these factors.

Methylformate (CH_3OCHO) appears as a mixture with H_2CO in the fits. Its pure form shows vibrational bands at 5.8 μm (C=O stretch), 8.26 μm (C–O stretch), 8.58 μm (CH_3 rocking), 10.98 μm (O–CH_3 stretch), and 13.02 μm (OCO deformation) (J. Terwisscha van Scheltinga et al. 2021). However, in the CH_3OCHO:H_2CO mixture, matrix interactions lead to band shifts and altered widths. The O–CH_3 stretching mode is blueshifted, and the OCO deformation mode also shifts in position. The CH_3 rocking mode at 8.58 μm overlaps with the CH_2 wagging mode of H_2CO at 8.49 μm, producing a blended, broader feature in this region. The C=O stretch at 5.8 μm overlaps with the strong H_2CO band, making it unreliable for column density estimation. Instead, the relatively stable C–O stretching mode at 8.26 μm is used to determine the column density of CH_3OCHO. The H_2CO column density is estimated using its feature near 8.02 μm.

Ethanol (CH_3CH_2OH) is identified in our fits as an H_2O mixture. The weaker vibrational modes at 7.24 μm (CH_3

symmetric deformation), 7.4–7.7 μm (OH deformation), and 7.85 μm (CH_2 torsion) fall in relatively clean spectral regions. However, its stronger bands at 9.17 μm (CH_3 rocking), 9.51 μm (CO stretch), and 11.36 μm (CC stretch) are blended with dominant ice features of H_2O, as well as the broad silicate feature at ∼9.7 μm. The 7.24 μm band of ethanol–water mixture is relatively easy to detect as H_2O induces a peak shift, making it a promising candidate for identification (J. Terwisscha van Scheltinga et al. 2018).

Acetic acid (CH_3COOH) shows absorption bands at 7.3 and 7.7 μm. In our fits, it appears as a mixture with H_2O, resulting in a broadened profile at 7.7 μm. This band overlaps to a certain extent with some bands of OCN^-, SO_2, CH_4, CH_3OCHO, CH_3CH_2OH, and HCOOH, whereas 7.3 μm falls rather in a clean region. However, the intensity of the 7.7 μm band is twice that of the 7.3 μm band and is used to determine its column density.

Acetaldehyde (CH_3CHO) is detected in our fits as part of an H_2O mixture in the ratio 1:10. It shows four significant absorption features in the 5.5–12.5 μm range, with the most prominent being the CO stretching mode at 5.8 μm. However, this band overlaps with other interstellar molecules like H_2CO, HCOOH, and NH_2CHO, making its identification challenging. Similarly, the 6.995 and 8.909 μm bands coincide with CH_3OH features, further complicating detection. The CH_3 symmetric deformation + CH wagging mode at 7.427 μm, which has minimal overlap with common ice components, is the most reliable for identifying it, and the same is used to calculate the column density.

4.3.4. Organic Refractories

The bottom-left panel in Figure 5 shows the significant presence of organic refractory materials, which contribute to the excess absorption dip in the 5–10 μm region of the observed optical depth, alongside the H_2O bending mode. These materials are refractories even at room temperature, having high molecular mass up to 200 amu, and contain several molecules, radicals, and other fragments. The organic refractories show broad absorption features spanning from ∼5.5 μm to ∼11 μm in the MIRI range, indicating the presence of various functional groups including carbonyl (C=O), hydroxyl (O–H), amine (N–H), and C–H bending modes. Notably, this spectral region also coincides with absorption bands of volatile organics such as COMs, including aldehydes, esters, carboxylic acids, and amides, leading to significant spectral blending. The overlapping absorption features contribute to the overall depth of the observed bands making it challenging to isolate individual molecular contributions. This necessitates the determination of the local continuum in order to accurately isolate the absorption features of volatiles, which is shown in W. R. M. Rocha et al. (2024).

The spectra of organic refractories are obtained by G. M. Muñoz Caro & W. A. Schutte (2003), who irradiated a 12 K mixture of H_2O:NH_3:CH_3OH:CO:CO_2 in the ratio 2:1:1:1:1 using a hard UV dose of 0.25 photon molecule^{-1}. The residue spectrum is shown in Figure 12. The strongest peak due to the –COO^- antisymmetric stretch of carboxylic acid salts [(R–COO^-)(NH_4^+)] is observed at around 6.3 μm. Hexamethylenetetramine (HMT) is also identified through the 8.10 (ν_{22}) and 9.93 (ν_{21}) μm stretch of CN. The peak at 9.21 μm characteristic of glycolic acid is due to ammonium glycolate. It also accounts for the 20% of the feature present at 6.30 μm due to the COO^- stretching mode. The rest is due to other acid salts like ammonium glycerate ($HOCH_2CH(OH)COO^-$)(NH_4^+) and ammonium oxamate (NH_2COCOO^-)(NH_4^+). The minor absorption features at 5.74 and 5.95 μm are attributed to the C=O stretching mode of esters (R–C(=O)–O–R′) and primary amides (R–C(=O)–NH_2), respectively. A weak band due to NH_2 deformation in primary amides arises between 6.06 and 6.17 μm , confirming the presence of primary amides.

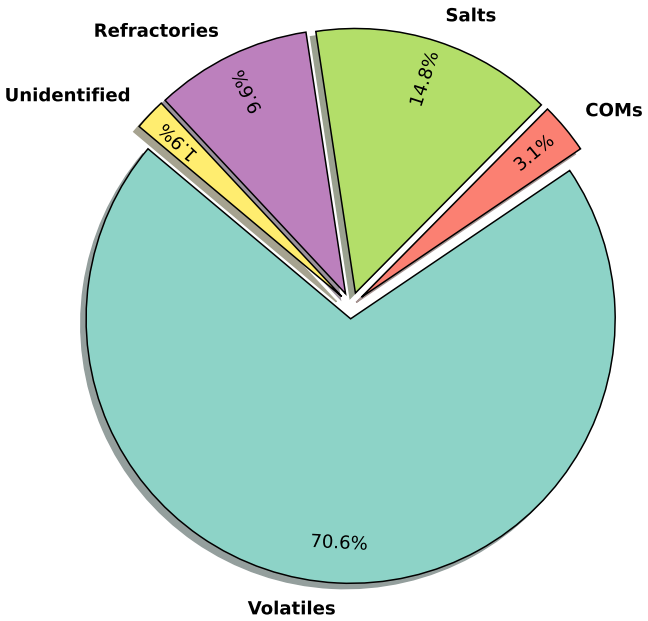

Figure 6. Percentage contribution to the spectral area of different ice groups in the 5–8 μm range. The model provides a good fit across the region as shown in Figure 4, except for the 7.1–7.5 μm interval. Appropriate polynomial baselines are used to separate the different ice groups present in the same ice mixture.

The model, which includes refractory material spectra, accurately reproduces the observed absorption features in the 5–10 μm region, particularly between 5 and 7.12 μm, with the exception of some localized mismatches between 7.1–7.5 μm and at 8.26 and 8.9 μm. We suspect the mismatch in the 7.1–7.5 μm region may arise from unidentified or missing components. Similarly, the deviations observed at 8.26 and 8.9 μm may be due to uncertainties in the baseline of refractory material spectra. To better understand the relative contributions of refractory materials and various ice types to the 5–8 μm optical depth spectrum, we estimate the percentage area covered by each ice group, as illustrated in Figure 6. Volatile ices dominate the absorption area (70.6%), followed by salts (14.8%), refractory organics (9.6%), and COMs (3.1%), and unidentified components constitute 1.9%. These findings highlight the importance of including organic refractory materials in the model to accurately reproduce the observed spectrum. The implications of refractory materials in astrophysical environments, including their formation efficiencies, are discussed further in Section 5.

4.4. Statistical Interpretation

Figure 7 presents the R^2 analysis of the spectral fitting process where components are added sequentially in descending order of their contribution, defined by the maximum optical depth of each component in the MIRI range. As shown in Figure 7, the first few components, mainly H_2O and CO_2 mixtures together with organic residues, play a dominant role

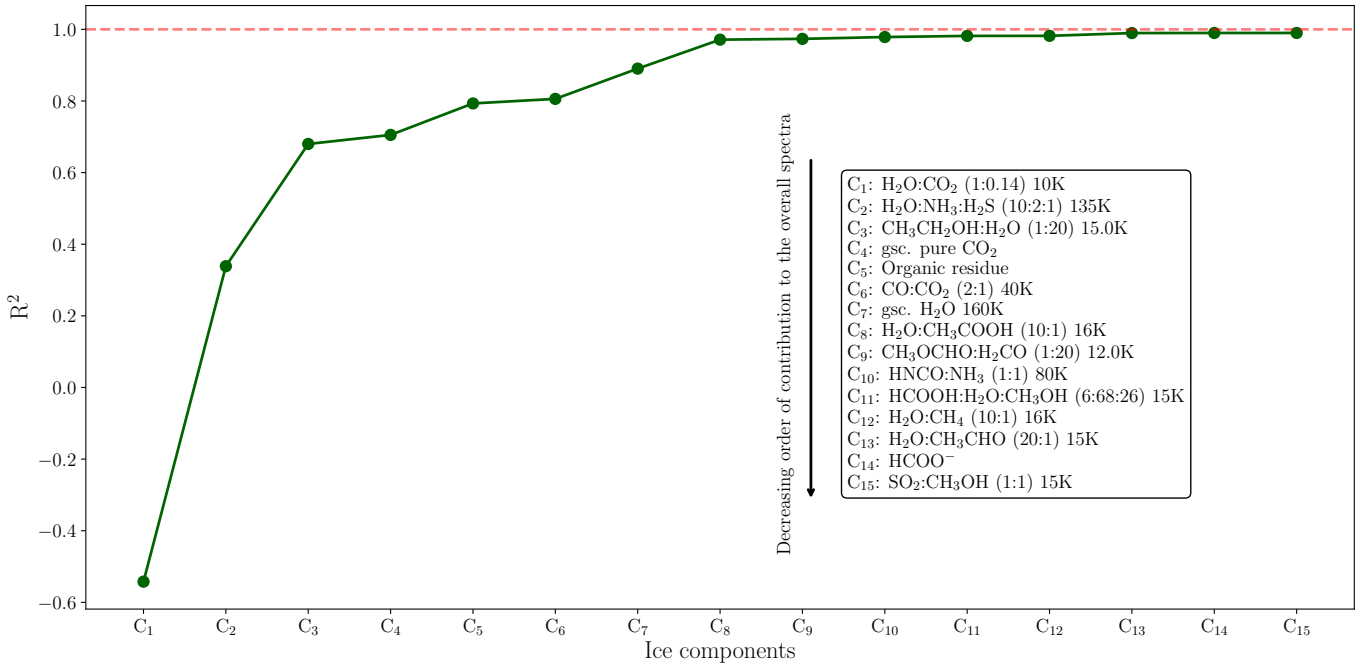

Figure 7. R^2 value as each component is added to the model. The R^2 for individual components is shown in green dots. The cumulative R^2, the normalized sum of cumulative R^2, is also plotted in blue dots to illustrate the relative change in R^2. Components are added in descending order of their contribution, which is defined as the maximum optical depth of the respective component.

in improving the fit and lead to a rapid increase in the R^2 value. These species are expected to be major constituents of interstellar and protostellar ices due to their observed abundance in astrophysical environments. The model accuracy improves significantly until the first eight components whose contribution to the optical depth spectrum exceeds at least 0.6 in optical depth units. Beyond this point, adding relatively minor components (contributing $\lesssim$0.6 optical depth units to the spectrum) yields only marginal improvements, indicating that the overall spectral profile is largely governed by a few dominant species.

To assess the significance of these minor components, we performed greedy backward elimination, *F*-tests, and *p*-tests. Among the 15 components included in the best-fit model, eight are dominant, while the remaining ones contribute mostly to localized features. As evident from Figure 7, the R^2 value stabilizes after the eighth component, suggesting weak contributions from additional components, COM ices. To further evaluate the impact of adding components, *p*-values calculated based on the χ^2 distribution remain consistently low ($\lesssim$0.05), indicating that these minor components are locally relevant. While computing statistical values, we consider only the "contributing region," defined as the wavelength range where the component's contribution exceeds the noise level (sigma). We have also performed an *F*-test to measure the extent to which each component is contributing, and the results are shown in Figure 8. All minor ice components have a significant influence on the spectral fitting and are essential to the fitting procedure. Among these, CH_3CHO contributes the most to the overall optical depth spectrum due to its association with H_2O bands, whereas the SO_2 mixture contributes the least, adding only $\sim$0.1 optical depth units in narrow local regions. Therefore, we included all of them in the final solution, as they were identified as relevant by the greedy backward elimination method. Each component contributes to the optical depth by more than 1σ, and their inclusion leads to a noticeable change in the model's relative variance, as evident from Figure 8.

4.4.1. Confidence Intervals

In Appendix D, we present the confidence intervals for the model components. Figures 16–18 show the correlations between components containing H_2O bands across three different spectral windows in the 5–20 μm range. The confidence contours indicate that all components contribute significantly to the fit. Most components show notable mutual correlations, reflecting the spectral overlap inherent to H_2O-rich mixtures. In particular, the H_2O:CH_3COOH and pure H_2O components display strong degeneracy, as evidenced by their elongated elliptical confidence contours, suggesting either spectral overlap or similar contributions within these windows. The H_2O:CH_3CHO component shows a large degree of uncertainty, as reflected in its broad and diffuse contour shapes.

Similarly, the CO_2-bearing components shown in Figures 19–21 show strong mutual correlations, again indicating significant spectral overlap. In particular, the H_2O:CO_2 mixture displays highly elongated confidence contours, pointing to substantial uncertainty in its contribution. The CO:CO_2 mixture and pure CO_2 components also show degeneracy, suggesting considerable spectral overlap, as illustrated in Figure 5. Additionally, the similar widths of their contours imply comparable contributions within the examined windows.

The correlation plots for components without H_2O and CO_2 bands are shown in Figures 22–24. These components, which include species such as HCOOH, CH_3OCHO, SO_2, $HCOO^-$, and complex organic residues, generally show weaker mutual correlations compared to the H_2O- and CO_2-bearing ices, suggesting more confined spectral contributions. Their confidence contours are typically compact and less elongated,

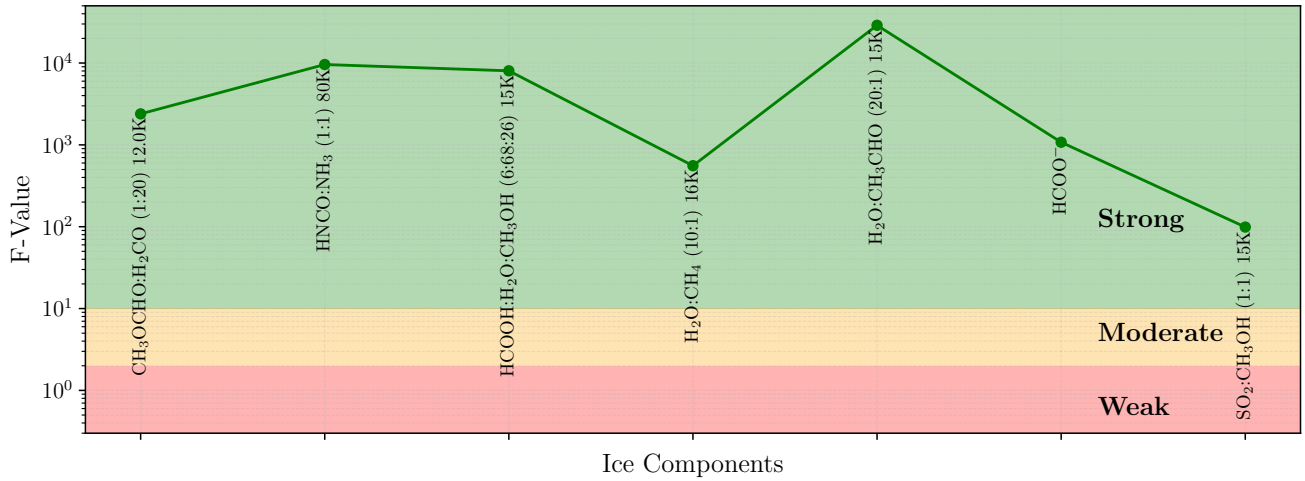

Figure 8. *F*-values for each minor ice component as it is sequentially added to the model, illustrating the relative change in variance. A higher *F*-value signifies a greater contribution of that component to the overall fit. Components are categorized as strong (in green region), moderate (in yellow region), or weak (in red region) based on the relative change in variance.

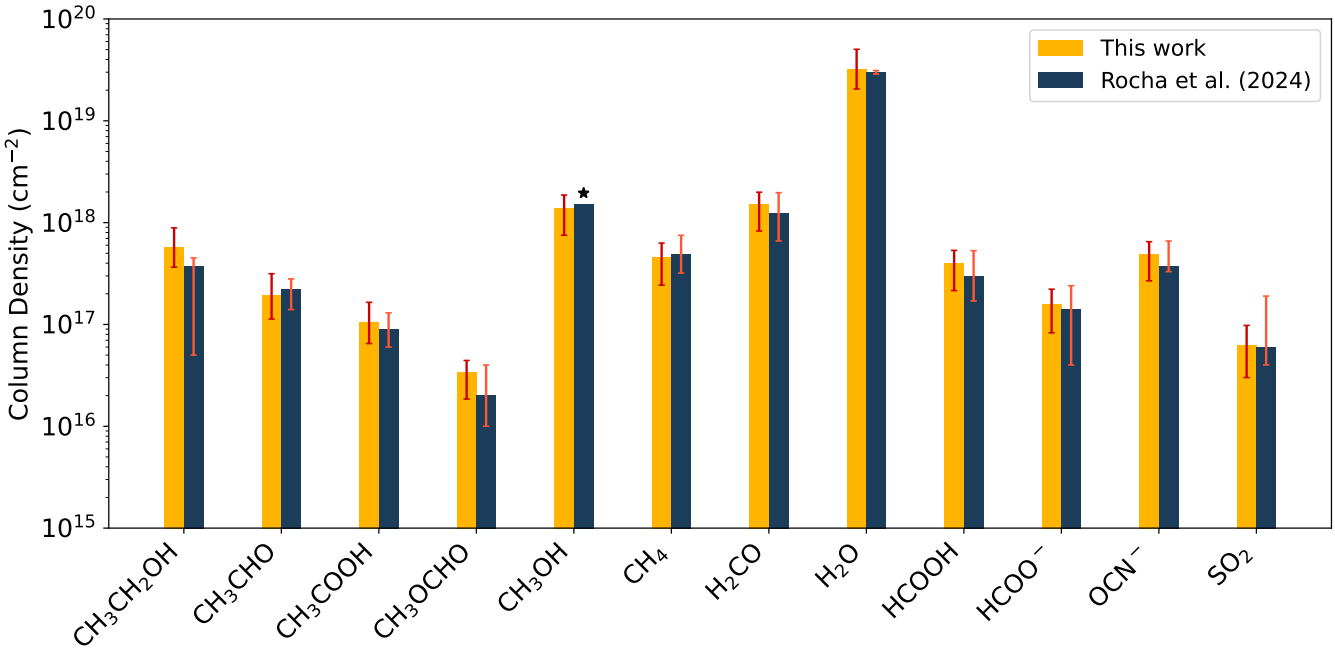

Figure 9. Comparison of ice column densities derived in this work (gold), using global fitting, with those from W. R. M. Rocha et al. (2024; dark blue), who used local fitting. The *x*-axis represents different ice species, while the *y*-axis shows the column densities in cm^2. Error bars, shown in red, indicate the uncertainties associated with each measurement. For CH_3OH, a factor of 2 or 3 is used in the two fitting methods denoted by a star. This agreement highlights the robustness of our global fitting approach using `INDRA` in capturing the ice inventory consistently with previous studies.

indicating lower degeneracy and more distinct contributions in this spectral region. The SO_2 mixture, however, shows considerable uncertainty within its region of influence.

4.5. Column Densities and Comparison with Local Fitting Results

The ice column densities of different species obtained through global fitting are presented in Table 5. For comparison, we also include column densities derived from local fitting by W. R. M. Rocha et al. (2024), shown in Figure 9. Additionally, abundances relative to H_2O observed toward various sources are presented in Table 5 and are compared in Figures 10 and 11. The column densities derived from global fitting fall within the ranges estimated by local fitting, indicating that both approaches yield consistent results. As shown in Figure 9, most ice species agree within a factor of 2 between the two methods, with the exception of $HCOO^-$, whose global fitting estimate is 2.6 times higher than the local fitting result.

This discrepancy in $HCOO^-$ can be interpreted in two ways. On one hand, the global fit includes its strong absorption band at 6.32 μm, which may support the higher estimate. On the other hand, the value could be overestimated due to fitting uncertainties in the 7.1–7.5 μm region, where missing components may lead the model to assign extra absorption to $HCOO^-$. A similar situation is observed for CH_3CH_2OH, which also shows a slightly higher estimate, though still within a factor of 2.

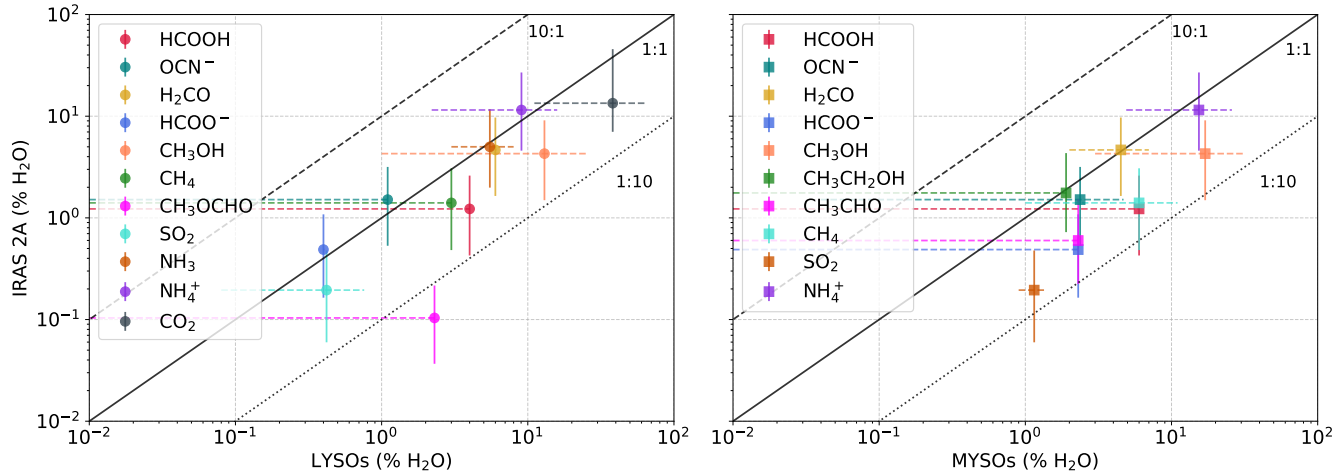

Figure 10. Comparison of ice abundances as a percentage of H_2O of IRAS 2A with those of LYSOs (left panel) and MYSOs (right panel). The solid line represents a 1:1 reference, while the dotted and dashed lines indicate abundances that are reduced and increased by a factor of 10, respectively. Table 5 lists the values used for the comparison of LYSOs and MYSOs with IRAS 2A.

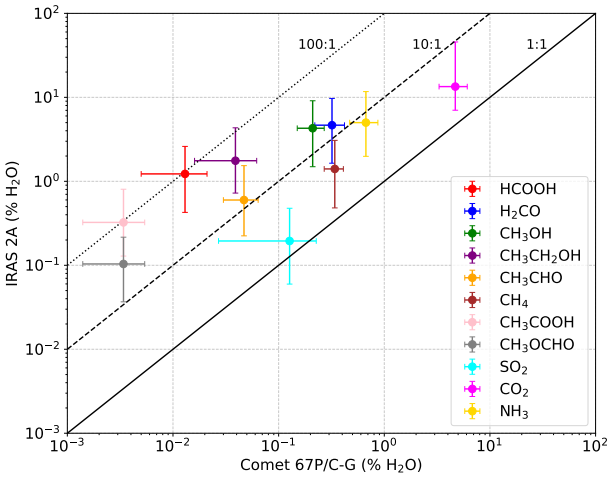

Figure 11. Comparison of ice abundances as a percentage of H_2O of IRAS 2A with those of comet 67P/C-G from M. Rubin et al. (2019). The solid line represents a 1:1 reference, while the dashed and dotted lines indicate cometary abundances that are reduced by factors of 10 and 100, respectively.

5. Discussions

5.1. Global versus Local Fitting

From Figure 9, it is evident that global and local fitting yield comparable column densities. In local fitting, the baseline is determined within a narrow spectral window requiring a precise knowledge of the placement of guiding points to anchor the continuum. This method is particularly sensitive to user-defined inputs and can result in the exclusion or misrepresentation of certain components. For example, W. R. M. Rocha et al. (2024) have shown in their Appendix J how the components such as CH_3CHO and CH_3COOH may be excluded from the fit solely due to the choice of guiding point placement. Since ice spectra contain overlapping absorption bands, determining the continuum placement can be challenging. However, global fitting relies on a single baseline across the entire spectral range and simultaneously considers multiple features of the same ice at different wavelengths. This approach ensures a more self-consistent decomposition of spectral components, reducing uncertainties associated with local continuum selection. For example, in the IRAS 2A optical depth spectrum, the absorption band due to OCN^- at 15.87 μm overlaps with CO_2 and H_2O, making it almost unrecognizable. In such cases, one might tend to attribute the entire absorption to CO_2 and H_2O ices, potentially overlooking the contribution from OCN^-. However, global fitting accounts for this issue by considering multiple spectral regions where OCN^- shows distinct features, ensuring that its contribution is properly constrained. Also, if the absorption features of different ices are not severely blended with dominant ones, regardless of whether the baseline is determined locally or globally, the overall column densities remain largely unaffected, as they are primarily dictated by the unique absorption strengths and intrinsic band profiles of ices, which is the case with CH_4, SO_2, and CH_3OH as shown in Figure 9. Another drawback of the local fitting approach is that it can disrupt physically meaningful correlations between absorption bands of the same species, potentially leading to inconsistent or unreliable estimates across those bands. For example, $HCOO^-$ shows an intense absorption band at 6.32 μm, which is nearly twice as strong as its weaker bands at 7.2 and 7.4 μm. Previous study that employed local fitting within the 6.8–8.6 μm region was limited to the weaker bands for column density estimation. As a result, these estimates may have been less reliable due to the lower band strengths. In contrast, the global fitting approach adopted in this work leverages the full MIRI range, allowing the inclusion of the stronger 6.32 μm feature. This leads to a more robust constraint on the $HCOO^-$ abundance, yielding column densities that are nearly twice those derived from the local fitting method. However, we caution that this higher value may also be influenced by the spectral gap in the model and observed spectrum due to the absence of certain components in the 7.1–7.5 μm region, which could lead the model to overfit $HCOO^-$ in the region.

5.2. Treatment of H_2O, CO_2, and CH_3OH Bands in Some of the Ice Mixtures

In our spectral fitting analysis, the presence of H_2O and CH_3OH bands in the ice mixtures alongside the features of COMs carries important physical implications. In general, the inclusion of H_2O and CH_3OH absorption features in ice mixtures provides compelling evidence that these species are embedded in H_2O- and CH_3OH-rich matrices, a condition supported by laboratory experiments. Therefore, our general approach has been to retain

Table 5
Ice Column Densities Obtained toward IRAS 2A Using Global Fitting Estimations Using INDRA and Local Fitting Results from W. R. M. Rocha et al. (2024)

Species	N_{ice} (10^{17} cm^{-2})		X_{H_2O} (%)		Literature (% H_2O)		
	Global	Local	Global	Local	LYSOs	MYSOs	Comet 67P/C-G[a]
H_2O (13 μm)	$324.00^{504.00}_{205.00}$	300 ± 12	100	100	100	100	100
HCOOH	$3.97^{5.34}_{2.15}$	$3.0^{5.3}_{1.7}$	1.23	1.0	$<0.5-4$[b]	$<0.5-6$[c]	0.013 ± 0.008
OCN^-	$4.90^{6.50}_{2.68}$	$3.7^{6.6}_{3.3}$	1.51	1.2	$<0.1-1.1$[d]	$0.04-4.7$[e]	...
H_2CO	$15.10^{19.90}_{8.28}$	$12.4^{19.7}_{6.6}$	4.66	4.1	~ 6[f]	$\sim 2-7$[g]	0.32 ± 0.1
$HCOO^-$ (7.4 μm)	$1.58^{8.27}_{2.22}$	$1.4^{2.4}_{0.4}$	0.49	0.15	~ 0.4[f]	$<0.3-2.3$[g]	...
CH_3OH	$13.88^{18.66}_{7.52}$[h]	15, 23[i]	4.28	5.0, 7.6	$<1-25$[c]	$<3-31$[c]	0.21 ± 0.06
CH_3CH_2OH	$5.70^{8.89}_{3.65}$	$3.7^{4.5}_{0.5}$	1.76	1.2	...	<1.9[j]	0.039 ± 0.023
CH_3CHO	$1.94^{3.15}_{1.13}$	$2.2^{2.8}_{1.4}$	0.60	0.7	...	<2.3[j]	0.047 ± 0.017
CH_4	$4.55^{6.30}_{2.43}$	$4.9^{7.5}_{3.2}$	1.40	1.6	<3[k]	$1-11$[g]	0.340 ± 0.07
CH_3COOH	$1.05^{1.65}_{0.65}$	$0.9^{1.3}_{0.6}$	0.32	0.3	...	...	0.0034 ± 0.002
CH_3OCHO	$0.34^{0.44}_{0.18}$	$0.2^{0.4}_{0.1}$	0.10	0.1	<2.3[l]	...	0.0034 ± 0.002
SO_2	$0.63^{0.98}_{0.30}$	$0.6^{1.9}_{0.4}$	0.19	0.2	$0.08-0.76$[k]	$<0.9-1.4$[g]	0.127 ± 0.100
New species found in this work							
Simple ice species							
NH_4^+	$37.30^{55.20}_{23.10}$[m]	...	11.51	...	$\sim 2.2-15.9$[f,n]	$\sim 4.9-28$[f,n]	...
CO_2 (15 μm)	$43.50^{93.60}_{35.40}$	...	13.43	...	$\sim 11.09-65.12$[o]	...	4.7 ± 1.4
NH_3	$16.20^{24.00}_{10.00}$	...	5.00	...	$\sim 3-8$[f]	...	0.67 ± 0.20
$NH_4^{+ö}$	0.75	...	0.23	...	$\sim 2.2-15.9$[f,n]	$\sim 4.9-28$[f,n]	...
HMT[p]	3.15	...	0.9	...	...	...	Negligible[q]
Carboxylic acid salt[p]	1.66	...	0.5	...	...	...	...
POM[p]	0.39	...	0.1	...	...	...	Negligible[q]
Amide[p]	0.21	...	0.06	...	...	...	...
Ester[p]	0.17	...	0.05	...	...	...	...

Notes. These values are compared to literature values for other objects.
[a] M. Rubin et al. (2019).
[b] K. I. Öberg et al. (2011).
[c] W. A. Schutte et al. (1999).
[d] F. A. Van Broekhuizen et al. (2005).
[e] A. C. A. Boogert et al. (2022).
[f] A. C. A. Boogert et al. (2008).
[g] E. L. Gibb et al. (2004).
[h] Values are reported with a factor of 2.
[i] Values are reported with a factor of 2 or 3.
[j] J. Terwisscha van Scheltinga et al. (2018).
[k] K. I. Öberg et al. (2008).
[l] J. Terwisscha van Scheltinga et al. (2021).
[m] Contributions from H_2O:NH_3:H_2S mixture, OCN^- ion salts.
[n] K. Slavicinska et al. (2025).
[o] K. M. Pontoppidan et al. (2008).
[p] Features belonging to organic refractory salt are shown separately as there are $\lesssim$20 % uncertainties in the estimates due to local baseline placements (G. M. Muñoz Caro & W. A. Schutte 2003).
[q] N. Hänni et al. (2022).
[r] M. G. Rachid et al. (2021).
[s] M. G. Rachid et al. (2022).
[t] K. Slavicinska et al. (2023).

these bands in ice mixtures wherever possible. However, exceptions were made in cases where the inclusion of dominant H_2O or CH_3OH bands introduced inconsistencies or degeneracy in the spectral fit, primarily due to overlapping contributions from different ice mixtures or uncertain baselines. In three of the COM mixtures, as listed in Table 4, we retain the H_2O bands to reflect the physical coexistence of H_2O and COMs in the ice matrix. The specific cases where dominant band removal was necessary are described below.

For the HCOOH:H_2O:CH_3OH (6:68:26) 15 K mixture, the spectrum near the 6 μm H_2O bending mode displayed a negative baseline as shown in the lower-left panel of Figure 14. After the baseline correction, the 6 μm band showed a significant improvement in its relative peak strength. Including the H_2O contribution from this mixture introduced inconsistencies in the modeled spectrum and adversely affected the stability of the fit. Given that H_2O is already well accounted for by other mixtures in the model, we removed the

H_2O bands from this component to ensure stability in the fitting.

For the H_2O:CH_4 (10:1) 16 K mixture, the observed feature near 7.7 μm in the IRAS 2A optical depth spectrum could be reliably reproduced only when the dominant H_2O bands from this mixture were excluded. Retaining these bands led to overfitting of water features that were already adequately modeled by other components, which degraded the quality of the overall fit in the region. The feature at 7.7 μm is shaped by the combined contributions of CH_4 (7.67 μm), SO_2 (7.60 μm), and the OCN^- ion (7.62 μm). The improved fit quality around this region can be observed in Figure 4, and the corresponding CH_4 column density estimation compared to the local fitting is shown in Figure 9.

For the SO_2:CH_3OH (1:1) 10 K mixture, isolation of the SO_2 feature was necessary due to the presence of a strong CH_3OH absorption band at 9.74 μm. In the optical depth spectrum of IRAS 2A, this band is already well addressed by the CH_3OH band from the HCOOH:H_2O:CH_3OH mixture. As a result, including the additional CH_3OH contribution from the SO_2 mixture introduced redundancy and led to the rejection of the component. To address this, we removed the CH_3OH band from this mixture, isolating the SO_2 signatures at 7.60 and 8.68 μm with the former band being relatively intense one. The column densities of SO_2 and CH_3OH are comparable with the local fitting case, and the same is shown in Figure 9.

Grain-shape corrections were applied exclusively to some pure H_2O and CO_2 ices, as these are dominant ices and they can interact with grains, which can affect the band shapes. In contrast, such corrections were not applied to weaker ice components, which are not susceptible to grain-shape effects (P. Ehrenfreund et al. 1996; E. Dartois 2006; E. Dartois et al. 2022; N. G. C. Brunken et al. 2025). For mixtures containing dominant bands (e.g., H_2O-rich mixtures), applying grain-shape corrections is not straightforward, as the effects depend on factors such as ice layer thickness, density, and the internal structure of the mixture. We also note that further experimental and modeling studies are needed to better understand the grain-shape effects on band shapes.

5.3. Formation Pathway of the Detected Ices

Using global fitting, we identified multiple ice components contributing to the observed optical depth of IRAS 2A. These include simple molecules like H_2O, CH_4, and NH_3, and ions such as OCN^- and NH_4^+, as well as COMs such as CH_3OH, CH_3OCHO, and HCOOH. Additionally, we noted the possible presence of organic refractory salts. In this section we discuss the formation pathways of these ices.

Simple molecules such as H_2O, CH_4, NH_3, and SO_2 form through a combination of gas-phase and grain-surface reactions in interstellar environments. Water ice primarily forms on dust grains through the hydrogenation of atomic oxygen (G. Molpeceres et al. 2018), while in warmer regions, gas-phase reactions involving oxygen and molecular hydrogen also contribute (A. E. Glassgold et al. 2009). Methane is produced via the stepwise hydrogenation of atomic carbon on grain surfaces, a process that occurs efficiently at low temperatures in dense molecular clouds (D. Qasim et al. 2020; T. Lamberts et al. 2022). Similarly, ammonia forms through successive hydrogenation of atomic nitrogen on icy dust grains (K. Hiraoka et al. 1995; H. Hidaka et al. 2011; G. Fedoseev et al. 2014), and in the gas phase through a series of ion-molecular reactions (E. Herbst & W. Klemperer 1973; G. B. I. Scott et al. 1997; G. Fedoseev et al. 2014). Sulfur dioxide, on the other hand, can originate from both gas-phase reactions and surface chemistry. These simple molecules act as fundamental building blocks for more complex ices, undergoing further processing as star and planet formation proceeds.

The IRAS 2A environment harbors several ionic species. Laboratory experiments have demonstrated that such ions can form under purely nonenergetic conditions, primarily through acid–base reactions within the ice. However, the contribution of energetic processing cannot be excluded completely. Among these ions, NH_4^+ forms in interstellar ices primarily through acid–base reactions involving NH_3 and strong acids such as HNCO (grain-surface product). A proton transfer can readily occur in the presence of the strongly nucleophilic NH_3 with even a modest energy input, such as a slight temperature increase or UV radiation (T. I. Hasegawa & E. Herbst 1993). The $HCOO^-$ ion is typically formed through acid–base reactions in interstellar ices. Additionally, it can also be produced through surface chemistry involving CO and OH radicals on interstellar grains or via energetic processing (e.g., UV irradiation or cosmic-ray-induced reactions) of ice mixtures containing H_2O, CO, and H_2CO molecules. OCN^- forms efficiently under interstellar conditions through acid–base reactions (P. A. Gerakines et al. 2025) or processes involving photolysis or irradiation of CO and NH_3 containing ices (R. L. Hudson et al. 2001). It has been observed in interstellar ices (R. J. A. Grim & J. M. Greenberg 1987; W. A. Schutte & R. K. Khanna 2003; F. A. Van Broekhuizen et al. 2004) and is the primary carrier of the interstellar XCN band. CH_3CHO and CH_3CH_2OH are chemically linked in interstellar ices. Laboratory studies have shown that hydrogen bombardment of CH_3CHO ice can produce CH_3CH_2OH via sequential hydrogenation through the $CH_3CH(OH)$ radical intermediate, and that this pathway can proceed with 22% efficiency at temperatures as low as 10 K through quantum tunneling (S. E. Bisschop et al. 2007; K. J. Chuang et al. 2020). However, this reaction has a relatively high activation barrier (R. Sivaramakrishnan et al. 2010; G. Fedoseev et al. 2022), and recent quantum chemical calculations suggest that CH_3CHO is comparatively resistant to direct hydrogenation to ethanol in icy environments (G. Molpeceres et al. 2025). Chemical modeling instead points to a dominant top-down surface pathway in which CH_3CH_2OH is converted to CH_3CHO via hydrogen abstraction (M. Jin et al. 2025), likely enhanced by the higher ice abundance of ethanol. The relative importance of these pathways, particularly under the warmer and more energetic conditions typical of protostellar environments, remains uncertain. Further experimental and modeling studies are needed to quantify their efficiencies. CH_3COOH in the interstellar medium may form through gas-phase processes involving species such as CH_3CO^+, H_2O, $CH_3OH_2^+$, and HCOOH (W. Huntress & G. Mitchell 1979; P. Ehrenfreund & S. B. Charnley 2000), though these pathways alone do not fully account for observed abundances (D. M. Mehringer et al. 1997; A. Remijan et al. 2002). Laboratory and theoretical studies suggest that grain-surface chemistry involving radicals like CH_3, HOCO, CH_3CO, and OD in irradiated ices is a more efficient and likely dominant formation route (C. J. Bennett & R. I. Kaiser 2007; A. Bergantini et al. 2018; A. Ahmad et al. 2020; N. F. Kleimeier et al. 2020). CH_3OCHO forms primarily through surface

reactions involving CH_3O and HCO radicals. These radicals originate from CO hydrogenation on icy dust grains, a process that occurs efficiently at low temperatures (∼10–20 K) (e.g., N. Watanabe & A. Kouchi 2002; G. W. Fuchs et al. 2009). During this sequence, CO is first hydrogenated to form H_2CO, which can further react with hydrogen to produce CH_3OH. Meanwhile, the CH_3O and HCO radicals, which are intermediates in this process, can recombine to form CH_3OCHO (e.g., K. J. Chuang et al. 2016; R. T. Garrod et al. 2022; Y. Chen et al. 2023).

The formation of COMs within icy mantles on dust grains is primarily driven by the condensation of volatile species such as H_2O, CO, CO_2, and NH_3 in dense molecular clouds (P. Caselli et al. 1999; A. C. A. Boogert et al. 2015). Upon exposure to UV radiation from YSOs or external cosmic sources, these ices undergo photodissociation, leading to the generation of reactive radicals. The recombination of these species results in the synthesis of more COMs, including HMT, ammonium salts of carboxylic acids, amides, esters, and polyoxymethylene (POM)-related species (E. L. Gibb et al. 2001; R. T. Garrod & E. Herbst 2006; K.-J. Chuang et al. 2017). H_2O ice plays a catalytic role in facilitating these reactions by promoting radical diffusion and stabilizing intermediates. Laboratory experiments confirm that UV photoprocessing of ice mixtures, such as H_2O:CH_3OH:NH_3:CO:CO_2 at temperatures of ∼12 K, significantly enhances the formation of refractory organic residues (G. M. Muñoz Caro & W. A. Schutte 2003). The transformation of these organics into nonvolatile refractory materials occurs through further energetic processing. Silicate grains, as suggested by Y. Y. He et al. (2024), can incorporate these organics within their interlayer spaces, preserving them as interstellar material evolves into larger interplanetary objects like asteroids and comets.

5.4. Contributions from a Polar Environment

We observed that most of the organics are associated with water, suggesting a polar environment, which is also consistent with previous work by W. R. M. Rocha et al. (2024). The presence of COMs such as CH_3CHO, CH_3CH_2OH, and CH_3COOH within an H_2O-rich ice matrix indicates that water plays a dominant role in shaping the chemical environment of IRAS 2A. Water, being highly polar, strongly influences the spectral band shapes of these molecules, leading to broader features and peak shifts compared to their absorption in apolar environments. Additionally, laboratory experiments have demonstrated that COMs in polar ice environments exhibit different spectral characteristics compared to those in apolar matrices, further supporting the H_2O-dominated nature of the ice. Observations from the JWST-Ice Age program (M. K. McClure et al. 2023) suggest that CH_3OH, the most abundant COM, commonly coexists with H_2O in cold prestellar clouds, which is also the case for IRAS 2A. This coexistence may point to the influence of polar interactions in shaping ice chemistry, although recent modeling by I. Jiménez-Serra et al. (2025) indicates that methanol formation is predominantly driven by CO hydrogenation, independent of the ice's polar or apolar nature. Furthermore, the experiments by G. M. Muñoz Caro & W. A. Schutte (2003) suggest the role of H_2O as a catalyst in the formation of large organic molecules at cryogenic temperatures, which ultimately leads to the formation of COMs and refractory materials. The significance of a polar environment is also supported by the fact that the observed 7.2 μm feature in the ISO spectrum toward W 33A was better reproduced by S. E. Bisschop et al. (2007) when HCOOH is present in a polar environment rather than in CO- or CO_2-dominated regions. We have also observed the HCOOH appearing as a tertiary mixture that includes H_2O. This highlights the importance of complex ice-phase interactions through surface reactions involving H, OH, and HCO radicals, primarily in polar environments rich in H_2O and CH_3OH. Altogether, the available evidence points toward a predominantly polar chemical environment in IRAS 2A, although further chemical modeling and laboratory experiments are needed to fully confirm this interpretation.

5.5. Astrophysical Importance of the Detected Ices

The detection of various ices in IRAS 2A provides crucial insights into the chemical composition and evolution of planetary objects. All the identified ices, which include H_2O, CH_4, NH_3, CO, CO_2, and COMs such as CH_3CHO, CH_3CH_2OH, and CH_3COOH, have previously been observed in different astrophysical environments. Figures 10 and 11 show the presence of various ice species and comparison of the ice estimates from this work with those found in LYSOs and MYSOs, as well as in comet 67P. Note the good agreement between the estimated ice column densities and the observations toward LYSOs in Figure 10. Most estimates lie within a factor of 10 except CH_3OCHO, which appears to be an outlier. However, it is important to note that this apparent discrepancy is based on a single observation reported by J. Terwisscha van Scheltinga et al. (2021). This study sets an upper limit of approximately 2.3% relative to H_2O for CH_3OCHO in the low-mass protostar HH 46. Unlike the gas phase, where CH_3OCHO has been detected toward numerous sources including molecular clouds, direct ice-phase identifications remain limited due to strong spectral blending with other species. So, given that the available ice-phase constraint is based on a single upper-limit measurement and that spectral blending complicates its identification, more comprehensive ice observations are needed before drawing firm conclusions about its abundance relative to H_2O in low-mass protostellar environments. The left panel of Figure 10 indicates that IRAS 2A's ice composition is broadly comparable to both LYSOs and MYSOs. The panel also suggests that IRAS 2A is chemically more similar to LYSOs, supporting its classification as a low-mass protostar in a relatively early evolutionary stage. However, further observational and modeling studies are needed to evaluate the chemical similarity. Figure 11 presents a similar comparison with observations from comet 67P (M. Rubin et al. 2019). If the ice inventory from earlier phases is inherited by cometary bodies without significant alteration, one would expect a one-to-one correlation, as indicated by the solid line in Figure 11. However, the fractional abundances of most species relative to water are systematically depleted in comet 67P compared to IRAS 2A. This suggests that ices inherited from earlier stages undergo substantial processing before being incorporated into cometary nuclei. Notably, the COMs and their precursors, such as HCOOH and H_2CO, exhibit the strongest depletion, by factors $\gtrsim$10 in comet 67P. In contrast, simpler volatiles like NH_3, SO_2, CH_4, and CO_2 fall within a range of ∼1–10. This pattern likely reflects the thermal, radiative processing of ices and outgassing of materials during the protostellar-to-disk transition and after, where fragile COMs are easily destroyed or converted, while

simpler volatiles can efficiently be recondensed at low temperatures. These findings support the view that chemical inheritance from the protostellar phase is neither complete nor direct, and that significant chemical evolution occurs between the early envelope stage and the comet formation.

The detection of ions like OCN^-, NH_4^+, and $HCOO^-$ in IRAS 2A indicates an active chemical evolution. These ions are primarily formed through proton transfer and acid–base reactions within the ice, although the contribution of energetic processing cannot be excluded. The presence of HCOOH in this ice mixture highlights a chemically rich environment where hydrogen bonding interactions and acid–base equilibria play a crucial role in stabilizing ions and shaping the observed spectral signatures. Additionally, the detection of various COMs and their strong spectral association with H_2O suggest that water ice is a key driver in their formation, either by acting as a chemical catalyst or through hydrogenation pathways that transform simpler molecules into more complex species. The polar nature of the ice environment influences COM formation by stabilizing reactive intermediates, enabling radical accumulation and recombination under energetic processing, and potentially modifying spectral band shapes, as seen in JWST observations. Further, the detection of CH_3COOH, HCOOH, and CH_3OH highlights their potential role in prebiotic chemistry. This supports the idea that IRAS 2A harbors a chemically dynamic and evolutionarily significant ice reservoir, with potential implications for the prebiotic chemistry inherited by nascent planetary systems.

The inheritance of the refractory organics by carbonaceous chondrites (CR and CM types) further strengthens the connection between interstellar ice chemistry and the complex organic inventory in planetary systems (G. Danger et al. 2024). Additionally, HMT is known to desorb around 40 K, and its possible presence in protostellar sources, such as IRAS 2A, could be a useful tracer of cold regions where thermal desorption is beginning to release COMs into the gas phase (T. Javelle et al. 2024). The detection of HMT in select carbonaceous chondrites (e.g., Murchison, Murray, and Tagish Lake) highlights its potential role in prebiotic chemistry, as its degradation can yield formaldehyde and ammonia, which are key ingredients for amino acid formation (Y. Oba et al. 2020). However, high-resolution mass spectroscopic data from the Rosetta mission at comet 67P did not confirm the presence of polymers like POMs or HMT, suggesting that thermal processing may have altered these materials in cometary environments (N. Hänni et al. 2022). The presence or absence of HMT in extraterrestrial materials remains a key question in astrobiology, as its detection could provide significant insight into the molecular pathways that link interstellar ice chemistry with the organic inventory of early planetary bodies. If HMT is widely present in primitive extraterrestrial materials, it could represent a crucial prebiotic reservoir. Furthermore, its possible presence in protostellar sources like IRAS 2A may serve as a valuable probe of early stage star-forming regions, shedding light on the survival and evolution of prebiotic molecules in cold astrophysical environments.

6. Conclusion

Based on the spectral fitting of IRAS 2A using a global continuum across the entire JWST MIRI range, along with a comparison of the derived column densities with local fitting values and those observed toward YSOs and comet 67P, the following conclusions can be drawn.

1. The agreement between our derived ice column densities using global fitting and those from previous studies (W. R. M. Rocha et al. 2024) that used local fitting confirms that global fitting can be performed with accuracy comparable to local fitting, demonstrating the robustness of our approach.
2. In complex ice spectra, absorption features of different species often overlap significantly with dominant ice features, making the identification of weaker components challenging, as seen in the case of an OCN^- feature blended with H_2O and CO_2 bands. Local fitting, which focuses on isolated spectral regions, may assign the blended features to more dominant species, leading to underestimation of minor components or overestimation of major components. In contrast, global fitting leverages multiple spectral regions where each species shows distinct features, ensuring a more accurate and constrained determination of ice composition.
3. The presence of broad absorption features from $\sim$5.5 to $\sim$11 μm suggests contributions from various functional groups, including carbonyl (C=O), hydroxyl (O–H), amine (N–H), and C–H bending modes, indicating the presence of organic refractory materials. These refractory organics are crucial for understanding irradiation-driven chemical evolution in star- and planet-forming regions, and are likely incorporated into comets, asteroids, and C-type chondrites.
4. The global fitting approach not only improves the accuracy of column density estimates by leveraging the full spectral range and all ice absorption bands but also reveals a rich chemical inventory. This includes simple volatiles such as H_2O, ionic species like NH_4^+, and COMs and their precursors, as well as refractory organic residues, which together highlight the chemical complexity of interstellar ices. These findings provide insights into the diverse physical and chemical processes at play in star-forming environments.
5. The spectral association of COMs with H_2O suggests that IRAS 2A hosts a predominantly polar environment. Furthermore, H_2O may actively influence COM chemistry, including the formation of organic refractory materials, by acting as a catalyst.
6. The good correlation of the estimated ice column densities of IRAS 2A with those of both LYSOs and MYSOs within a factor of 10 suggests a chemically linked evolutionary pathway, with IRAS 2A likely representing an early or intermediate stage of an LYSO.
7. The systematic depletion of COMs and, to some extent, simple volatiles in the cometary ices of 67P relative to H_2O suggests that ices inherited from earlier protostellar phases undergo significant thermal and radiative processing, outgassing, and chemical transformation. This implies that the inheritance of pristine ices is incomplete and that ice compositions are actively reprocessed both prior to and after incorporation into cometary bodies.

Acknowledgments

P.R. and L.M. express their sincere thanks to Ewine F. van Dishoeck for detailed discussions related to the development

of INDRA and for sharing her valuable feedback, which significantly improved the results and discussions presented in the paper. P.R. and L.M. especially thank Katie Slavicinska for sharing NH_4SH ice spectroscopy data, which have been used in the INDRA global fitting. L.M. also thanks the JOYS+ team members for their enthusiastic comments, which have helped improve the capabilities of INDRA over time. L.M. further thanks Murthy Gudipati for insightful discussions on ice spectroscopy. L.M. acknowledges financial support from DAE, Government of India, which enabled this work. This research was carried out in part at the Jet Propulsion Laboratory, California Institute of Technology, under a contract with the National Aeronautics and Space Administration (NASA). Also, special thanks to the Astrochemistry group in Leiden, which is supported by the Netherlands Research School for Astronomy (NOVA), by funding from the European Research Council (ERC) under the European Union's Horizon 2020 research and innovation program (grant agreement No. 101019751 MOLDISK), by the Dutch Research Council (NWO) grants TOP-1 614.001.751 and 618.000.001, and by the Danish National Research Foundation through the Center of Excellence "InterCat" (grant agreement No. DNRF150). K.W. acknowledges financial support from the NASA Emerging Worlds grants 18-EW-18_2-0083 and 22-EW22-0033. Observations for this study were carried out using the James Webb Space Telescope (JWST), a joint mission of NASA, ESA, and CSA. The data were accessed via the Mikulski Archive for Space Telescopes (MAST) at the Space Telescope Science Institute, operated by the Association of Universities for Research in Astronomy, Inc., under NASA contract NAS 5-03127. The dataset corresponds to JWST program #1236 and is available via doi:10.17909/pgt6-5379. We would like to thank the anonymous referee for constructive comments that helped improve the manuscript.

Appendix A
List of Laboratory Data

Table 6 presents the laboratory ice components used in the ice-fitting analysis of IRAS 2A in the 5–28 μm region. These data were compiled from various databases, as indicated in the table and discussed in Section 3.3. In total, 76 ice spectra are included, consisting of both pure ices and mixtures with defined proportions. For species measured at multiple temperatures, we provide a single entry indicating the corresponding temperature range, rather than listing each spectrum separately. To improve the spectral fits and maintain physical consistency, we used grain-shape-corrected laboratory data for pure H_2O and CO_2 ices, obtained from W. R. M. Rocha et al. (2024) and K. M. Pontoppidan et al. (2008), respectively. Further discussion of grain-shape effects and correction methods can be found in P. Ehrenfreund et al. (1996), E. Dartois (2006), E. Dartois et al. (2022), and N. G. C. Brunken et al. (2025).

Table 6
Laboratory Data Used in This Work

Component	Absorption Features[a]	Ratio	T (K)	Database	References
pure H_2O[b]	H_2O	⋯	15–160	LIDA	K. I. Öberg et al. (2007)
pure H_2O UV irr.	H_2O	⋯	10–10.2	LIDA	P. Gerakines et al. (1996)
H_2O:CH_4	CH_4	10:1	15–16	UNIVAP	W. R. M. Rocha et al. (2017)
H_2O:CH_4	CH_4	10:0.6	16	UNIVAP	W. R. M. Rocha et al. (2017)
NH_3:CH_3OH	NH_3, CH_3OH	1:1	15	UNIVAP	W. R. M. Rocha et al. (2020)
H_2O:CH_3CHO	H_2O, CH_3CHO	20:1	15–120	LIDA	J. Terwisscha van Scheltinga et al. (2018)
pure CH_3CHO	CH_3CHO	⋯	15–120	LIDA	J. Terwisscha van Scheltinga et al. (2018)
pure $HCOOCH_3$	$HCOOCH_3$	⋯	15–120	LIDA	J. Terwisscha van Scheltinga et al. (2021)
CH_3CH_2OH:H_2O	CH_3CH_2OH, H_2O	1:20	15–160	LIDA	J. Terwisscha van Scheltinga et al. (2018)
CH_3CN	CH_3CN	⋯	15–150	LIDA	M. G. Rachid et al. (2022)
H_2O:CO_2	CO_2	1:0.14	10	LIDA	P. Ehrenfreund et al. (1997)
CO:CO_2	CO_2	2:1	15–130	LIDA	W. A. Schutte et al. (1999)
pure CO_2[b]	CO_2	⋯	⋯	⋯	K. M. Pontoppidan et al. (2008)
H_2O:NH_3:HCOOH	$HCOO^-$	100:2.6:2	14	LIDA	O. Gálvez et al. (2010)
H_2O:CH_3COOH	H_2O, CH_3COOH	10:1	16	NASA	NASA Cosmic Ice Laboratory[c]
H_2O:CH_3OH:NH_3:CO:CO_2	Org. res.[d]	2:1:1:1:1	12	⋯	G. M. Muñoz Caro & W. A. Schutte (2003)
HCOOH:H_2O:CH_3OH	HCOOH, CH_3OH	6:68:26	15	LIDA	S. E. Bisschop et al. (2007)
HNCO:NH_3	OCN^-	1:1	80	LIDA	J. H. Novozamsky et al. (2001)
pure CH_4	CH_4	⋯	12.0	OCdb	D. M. Hudgins et al. (1993)
CH_3COCH_3:H_2O	CH_3COCH_3	1:20	15	LIDA	M. G. Rachid et al. (2020)
CH_3COCH_3:H_2CO	CH_3COCH_3, H_2CO	1:20	15–150	LIDA	J. Terwisscha van Scheltinga et al. (2021)
pure SO_2	SO_2	⋯	10.0	LIDA	A. C. A. Boogert et al. (1997)
SO_2:CH_3OH	SO_2	1:1	10	LIDA	A. C. A. Boogert et al. (1997)
H_2O:NH_3:H_2S	H_2O, NH_4^+, NH_3	10:2:1	135	LIDA	K. Slavicinska et al. (2025)

Notes.
[a] Only the absorption features of the ice components for the listed species are included in the database.
[b] Grain-shape-corrected ices. Abbreviations: irr. = irradiated ice.
[c] NASA Cosmic Ice Laboratory reference spectrum for CH_3COOH: https://science.gsfc.nasa.gov/691/cosmicice/spectra/refspec/Acids/CH3COOH/ACETIC-W.txt.
[d] Organic residue consists of species with diverse functional groups including carbonyl (–C = O), carboxylate ($–COO^-$), amine ($–NH_2$), and –CN containing species. They also consist of carboxylic acid salts, hexamethylenetetramine (HMT) and polyoxymethylene (POM).

Appendix B
A Note on the Band Strengths of Ices Used in this Work

The band strengths of molecular ices vary significantly depending on whether they exist in a pure or mixed state. This is due to the intermolecular interactions that alter the vibrational properties of molecules. In pure ices, absorption features arise from the vibrational modes of individual molecules, which in fact depend on molecular dipole moment and crystalline structure, etc. However, when molecules are present as mixtures, interactions with other species can lead to shifts in band positions, changes in intensity, and modifications of band profiles. Consequently, there can either be enhancement or suppression of vibrational modes depending on the nature and strength of that interaction. The latter depends on the physical conditions like temperature as well. For example, J. Bouwman et al. (2007) found that, in H_2O:CO ice mixtures, band intensities vary systematically with concentration, with H_2O features weakening and the free OH stretch strengthening as CO increases. M. Bouilloud et al. (2015) have derived the correction factors for the band strengths of CO and CO_2 ices based on the works of P. A. Gerakines et al. (1995). Such variations in band strengths of ices can impact the ice column density estimations. And hence it is required to correct the band strengths of ices in order to prevent under- or overestimation of abundances. Table 7 lists band strengths of various ices used in this work along with their references.

Table 7
List of Vibrational Transitions and Band Strengths of Molecules Considered in This Paper

Chemical Formula	Name	λ (μm)	ν (cm^{-1})	Identification	$\mathcal{A}$ (cm $molecule^{-1}$)	References
H_2O	Water	13.20	760	libration	3.2×10^{-17}	(1, 14)
CH_4	Methane	7.67	1303	CH_4 def.	8.4×10^{-18}	(1, 2, 14)
SO_2	Sulfur dioxide	7.60	1320	SO_2 stretch.	3.4×10^{-17}	(2)
H_2CO	Formaldehyde	8.04	1244	CH_2 rock.	1.0×10^{-18}	(1)
CH_3OH	Methanol	9.74	1026	C−O stretch.	1.8×10^{-17}	(1)
…	…	…	…	…	1.56×10^{-17}	(15)
HCOOH	Formic acid	8.22	1216	C−O stretch.	2.9×10^{-17}	(1)
CH_3CHO	Acetaldehyde	7.41	1349	CH_3 s-def./CH wag.	4.1×10^{-18}	(3, 17)
CH_3CH_2OH	Ethanol	7.23	1383	CH_3 s-def.	2.4×10^{-18}	(4)
CH_3OCHO	Methyl formate	8.25	1211	C−O stretch.	2.52×10^{-17}	(5)
…	…	…	…	…	2.28×10^{-17}	(5)
CH_3COOH	Acetic acid	7.82	1278	OH bend.	4.57×10^{-17}	(6)
$HCOO^-$ (B1)	Formate ion	7.23	1383	C−H def.	8.0×10^{-18}	(16)
$HCOO^-$ (B2)	Formate ion	7.38	1355	C−O stretch.	1.7×10^{-17}	(16)
OCN^-	Cyanate ion	7.62	1312	Comb. ($2\nu_2$)	7.45×10^{-18}	(6)
NH_4^+	Ammonium ion	6.85	1428	ν_4 (asym. bend.)	4.4×10^{-17}	(11)
NH_3	Ammonia	9.34	1070	Umbrella mode	2.1×10^{-17}	(1)
CO_2	Carbon dioxide	15.27	654	…	$1.45 \times 1.6 \times 10^{-17}$[a]	(12)
HMT	Hexamethylenetetramine	8.1	1234	CN stretch.	2.6×10^{-18}	(13)
HMT	Hexamethylenetetramine	9.3	1007	CN stretch.	5×10^{-18}	(13)
CAsalt	Carboxylic acid salt	6.3	1586	…	6×10^{-17}	(13)
Amide	Amide	5.9	1680	…	3.3×10^{-17}	(13)
Ester	Ester	5.74	1742	…	2×10^{-17}	(13)
POM	Polyoxymethylene	9.1	1098	…	9.7×10^{-18}	(13)

Notes. Abbreviation of vibrational modes: def. = deformation; stretch. = stretching; s-def. = symmetric deformation; rock. = rocking; sym. = symmetric; asym. = asymmetric; Comb. = combination; wag. = wagging; bend. = bending; CAsalt = carboxylic acid salt; HMT = hexamethylenetetramine; POM = polyoxymethylene.

[a] Correction factor derived from M. Bouilloud et al. (2015) and N. G. C. Brunken et al. (2024).

References. (1) M. Bouilloud et al. (2015), (2) A. C. A. Boogert et al. (1997), (3) R. L. Hudson & R. F. Ferrante (2020), (4) N. Boudin et al. (1998), (5) J. Terwisscha van Scheltinga et al. (2021), (6) W. R. M. Rocha et al. (2024), (7) M. G. Rachid et al. (2020), (8) M. G. Rachid et al. (2021), (9) K. Slavicinska et al. (2023), (10) R. L. Hudson et al. (2005), (11) W. A. Schutte & R. K. Khanna (2003), (12) P. A. Gerakines et al. (1995), (13) G. M. Muñoz Caro & W. A. Schutte (2003), (14) D. M. Hudgins et al. (1993), (15) R. Luna et al. (2018), (16) W. A. Schutte et al. (1999), (17) J. Terwisscha van Scheltinga et al. (2018).

Appendix C
Baseline Corrections

In spectroscopic analysis, local baseline correction is essential for accurately extracting individual absorption features, especially when multiple components contribute to a broad spectral profile. Many ices produce overlapping absorption bands, leading to blended features that obscure individual contributions. In some cases, as in the case of organic molecules, the presence of strong, broad absorption bands from dominant species, say H_2O, can mask weaker features, making their fitting unreliable. By applying a local baseline correction, we can effectively remove underlying continuum variations and overlapping absorptions, ensuring that the extracted spectral features accurately represent the ices of interest. Polynomial baselines are effective in tracing the local continuum, and this approach is widely used in many studies (G. M. Muñoz Caro & W. A. Schutte 2003; Y. Chen et al. 2024; W. R. M. Rocha et al. 2024). This approach helps in determining ice column densities, and enhances the reliability of spectral fitting. Figures 12–15 show the local baseline corrections applied to various ice mixtures that are subsequently used in this work.

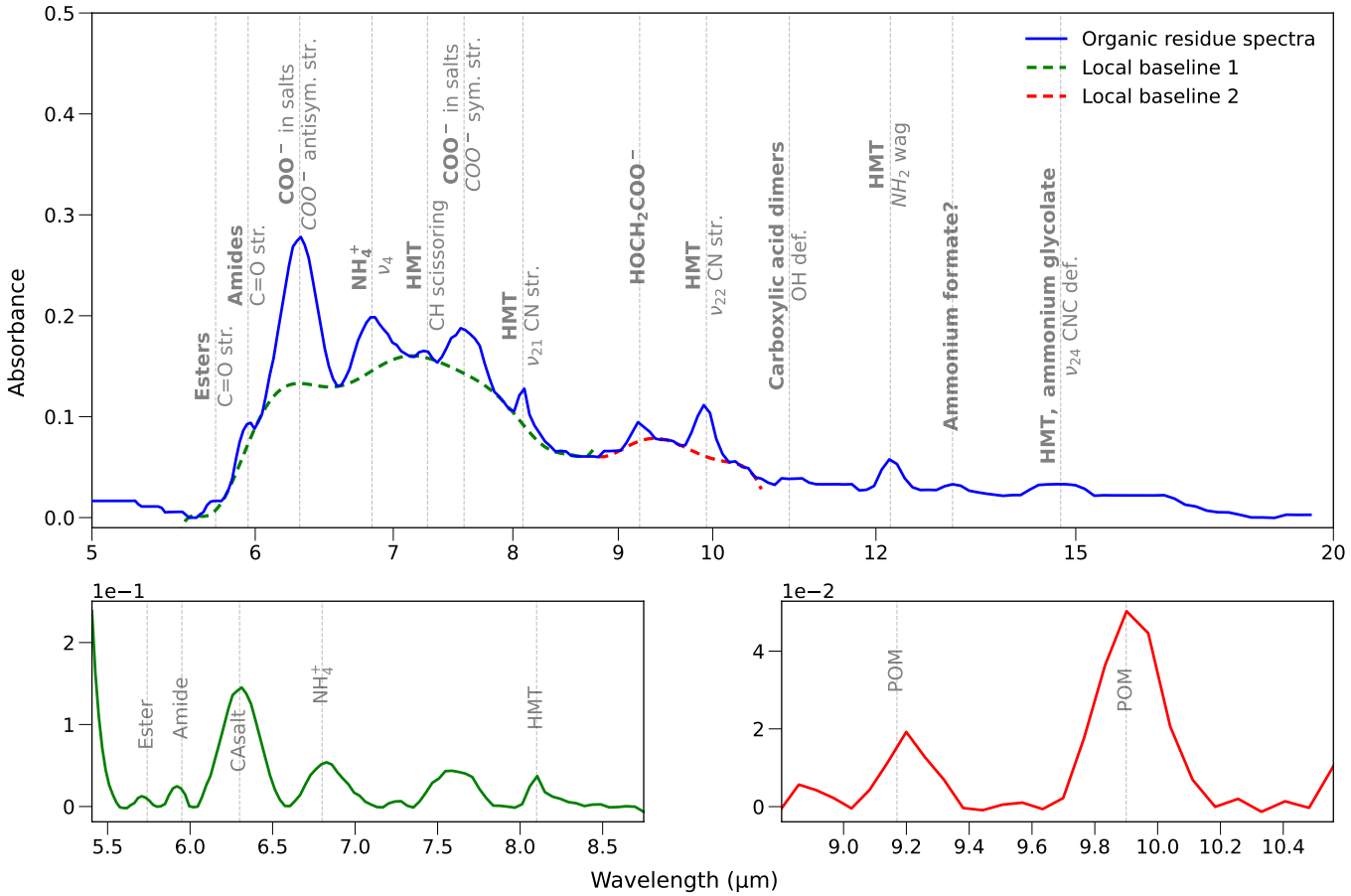

Figure 12. IR spectrum of the residue (blue) from the irradiated ice mixture H_2O:NH_3:CH_3OH:CO:CO_2 (2:1:1:1:1) at 12 K, adapted from G. M. Muñoz Caro & W. A. Schutte (2003). The top panel shows the spectrum in the 5–20 μm region, along with local polynomial baselines (dashed lines) used to isolate absorption features. These features are also indicated by labels in the text and gray dotted lines. They correspond to functional groups such as carbonyl (–C=O), carboxylate (–COO^-), amine (–NH_2), and –CN containing species. Because these features are blended within a broad profile, local baselines were required for accurate column density calculations. The bottom panel shows the baseline-corrected features (solid lines). Column densities were estimated using Equation (12) and band strengths listed in Appendix B. Uncertainties due to baseline selection are $\lesssim$20%. See G. M. Muñoz Caro & W. A. Schutte (2003) for details. Abbreviations: CAsalt = carboxylic acid salt; HMT = hexamethylenetetramine; POM = polyoxymethylene.

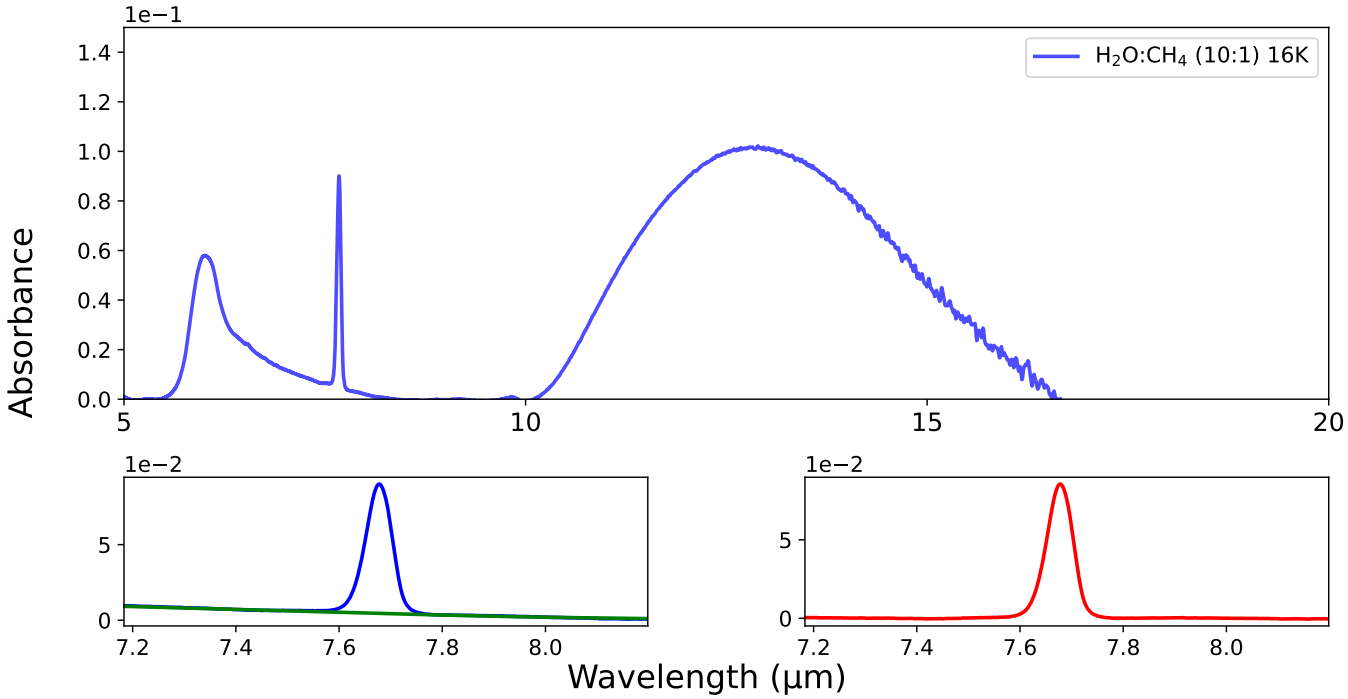

Figure 13. The absorption profile of H_2O:CH_4 (10:1) ice mixture (W. R. M. Rocha et al. 2017) is shown in blue. The bottom-left shows the CH_4 bending mode at 7.6 μm in blue and the corresponding local polynomial baseline in green. The resultant isolated band of CH_4 is shown in red.

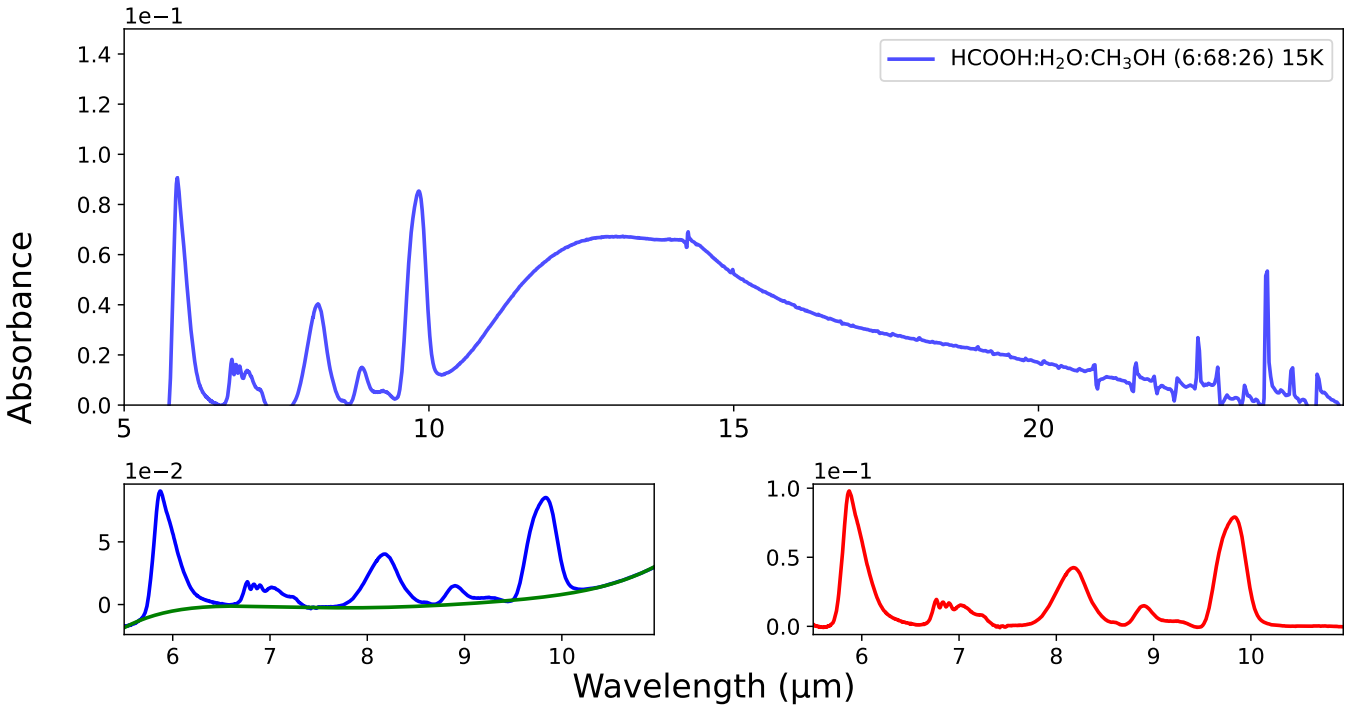

Figure 14. The absorption profile of 15 K ice mixture HCOOH:H_2O:CH_3OH (6:68:26; S. E. Bisschop et al. 2007) is shown in blue in the top panel. Features other than H_2O are shown in the bottom-left panel in blue and the corresponding polynomial baseline in green. The H_2O subtracted spectrum is shown in red.

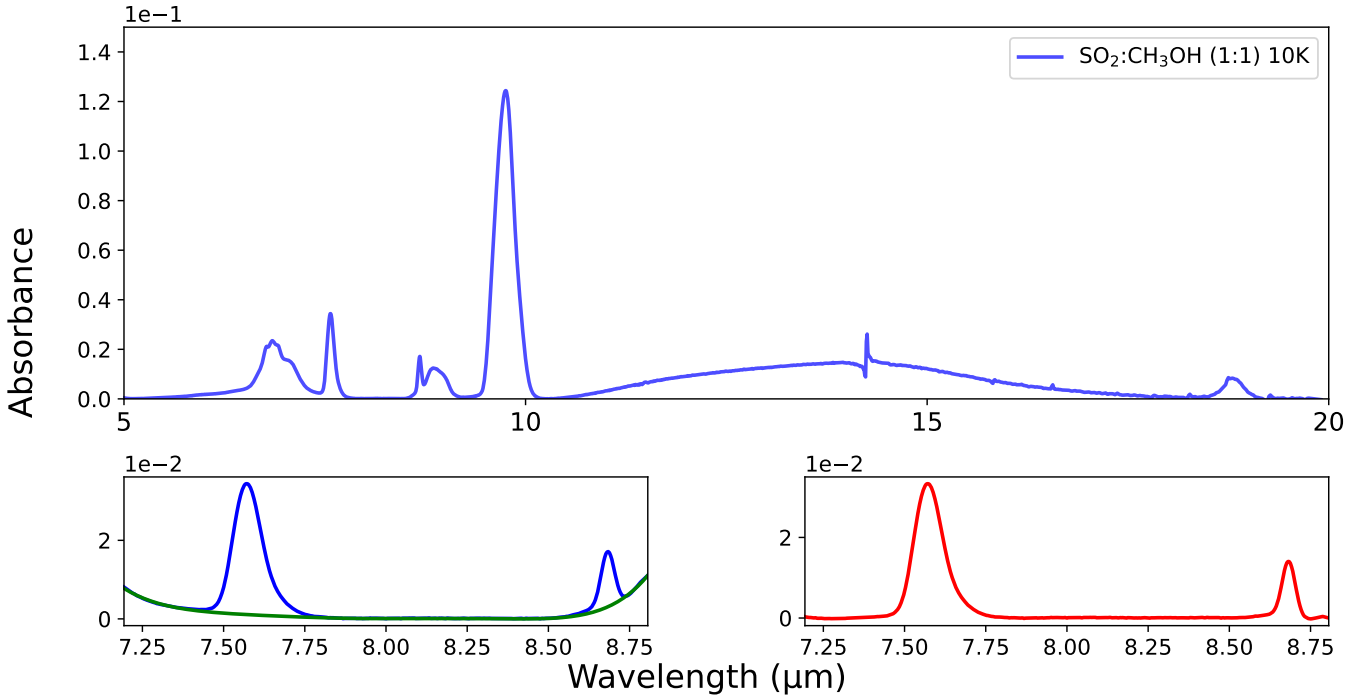

Figure 15. The absorption profile of SO_2:CH_3OH (1:1) 10 K ice mixture is shown in blue. The bottom-left panel shows the SO_2 features at 7.57 and 8.68 μm in blue and the corresponding local polynomial baseline in green. The resultant baseline-corrected profiles are shown in red in the bottom-right panel.

Appendix D
Statistical Results

Figures 16–24 show the correlation between different components across MIRI range using confidence interval analysis.

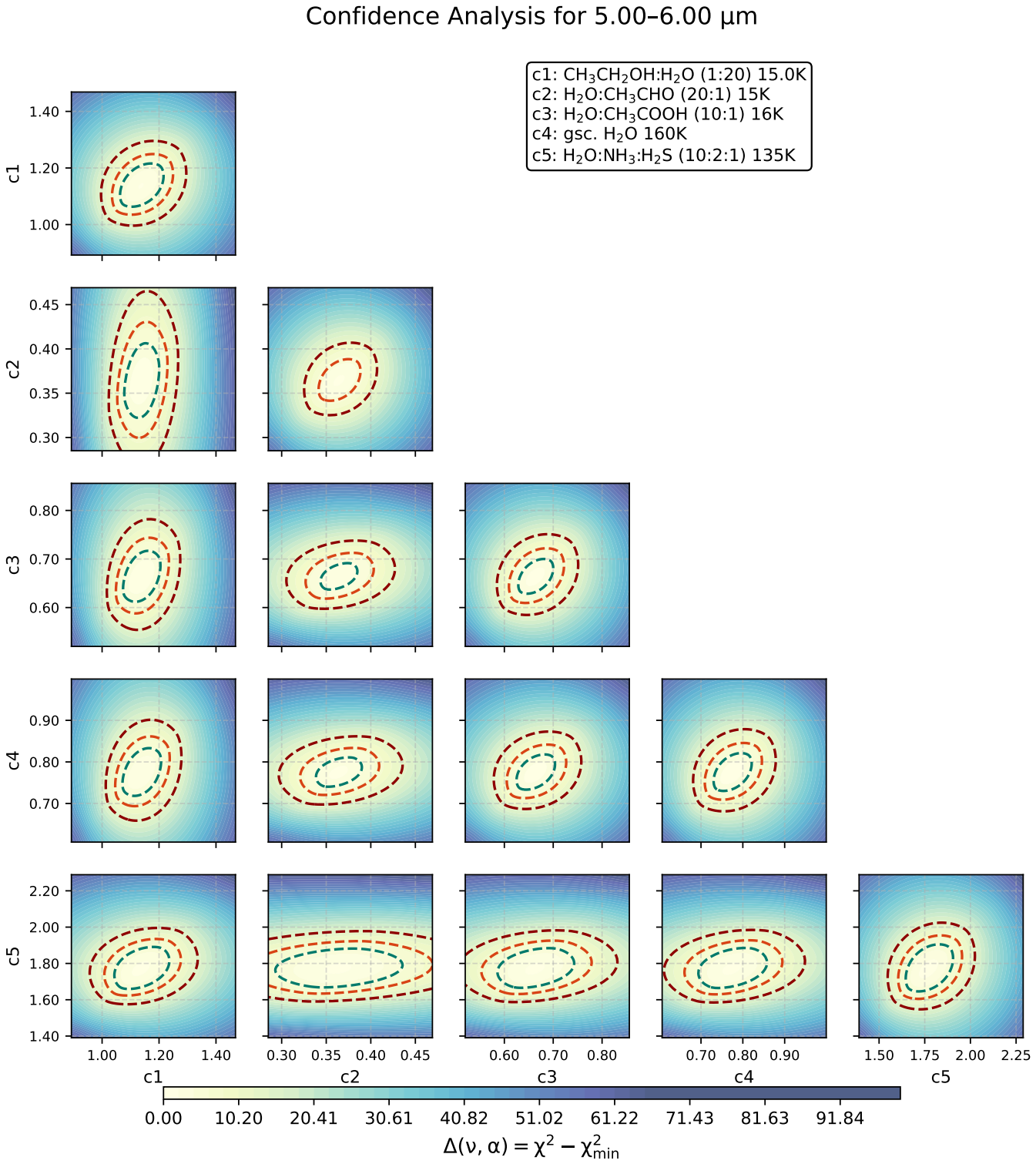

Figure 16. Confidence interval analysis of the components having H_2O bands based on χ^2 contributing in the 5–6 μm region. The blue, red, and brown dotted lines indicate the 1σ, 2σ, and 3σ levels. The coefficients of the remaining components are kept constant while performing this analysis.

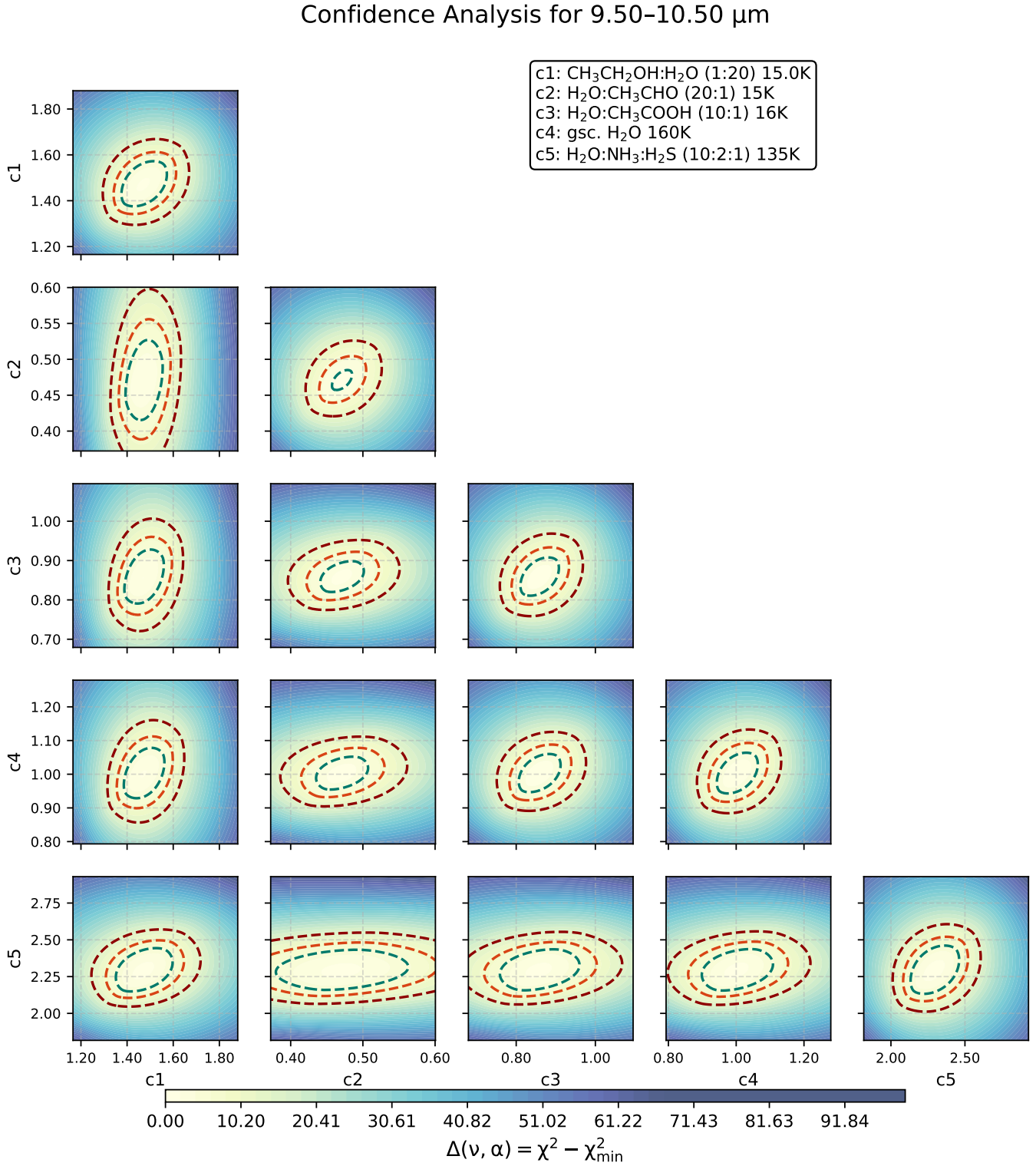

Figure 17. Confidence interval analysis of the components having H_2O bands based on χ^2 that are contributing in the 9.5–10.5 μm region. The blue, red, and brown dotted lines indicate the 1σ, 2σ, and 3σ levels. The coefficients of the remaining components are kept constant while performing this analysis.

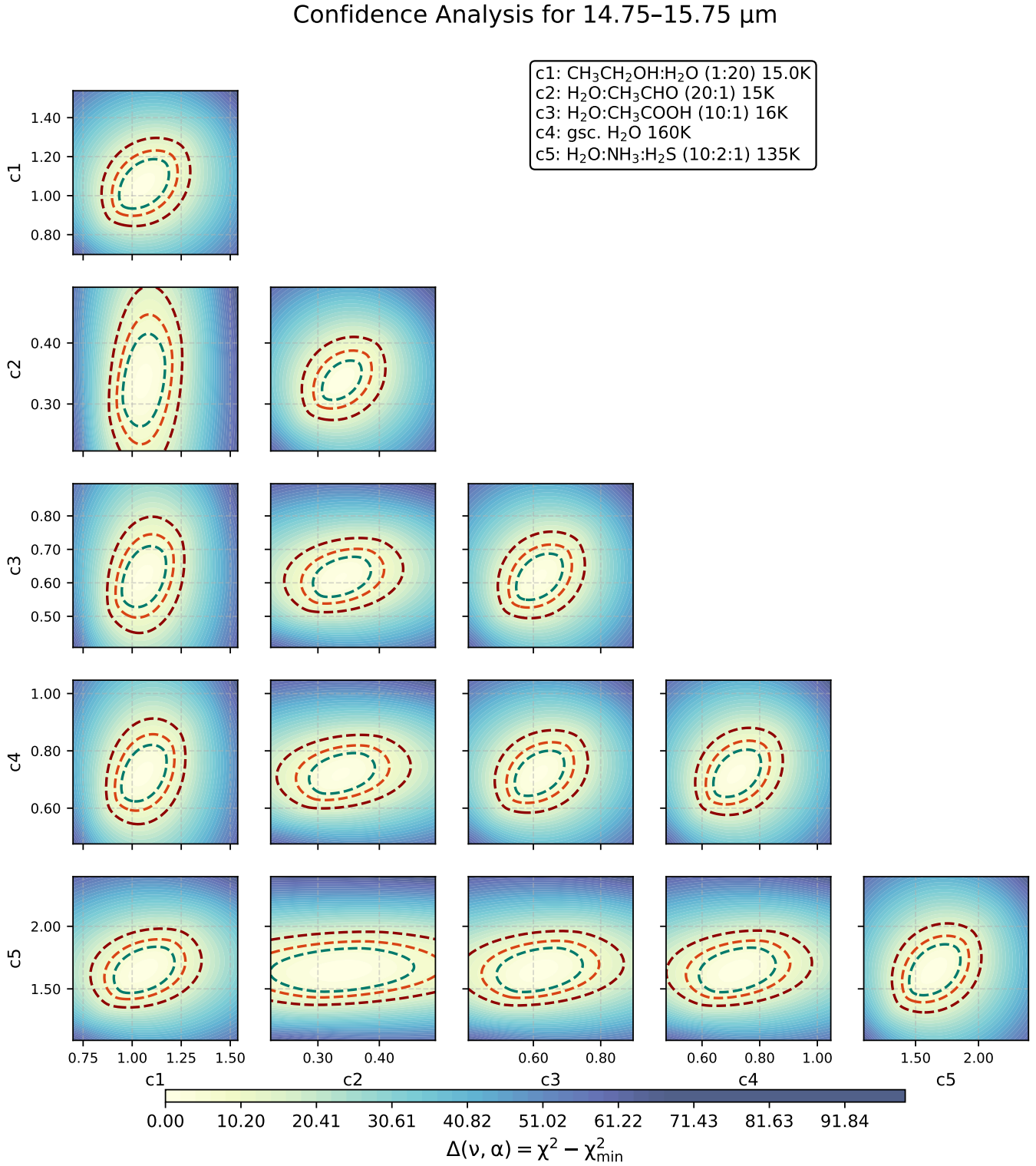

Figure 18. Confidence interval analysis of the components having H_2O bands based on χ^2 in the 14.75–15.75 μm region. The blue, red, and brown dotted lines indicate the 1σ, 2σ, and 3σ levels. The coefficients of the remaining components are kept constant while performing this analysis.

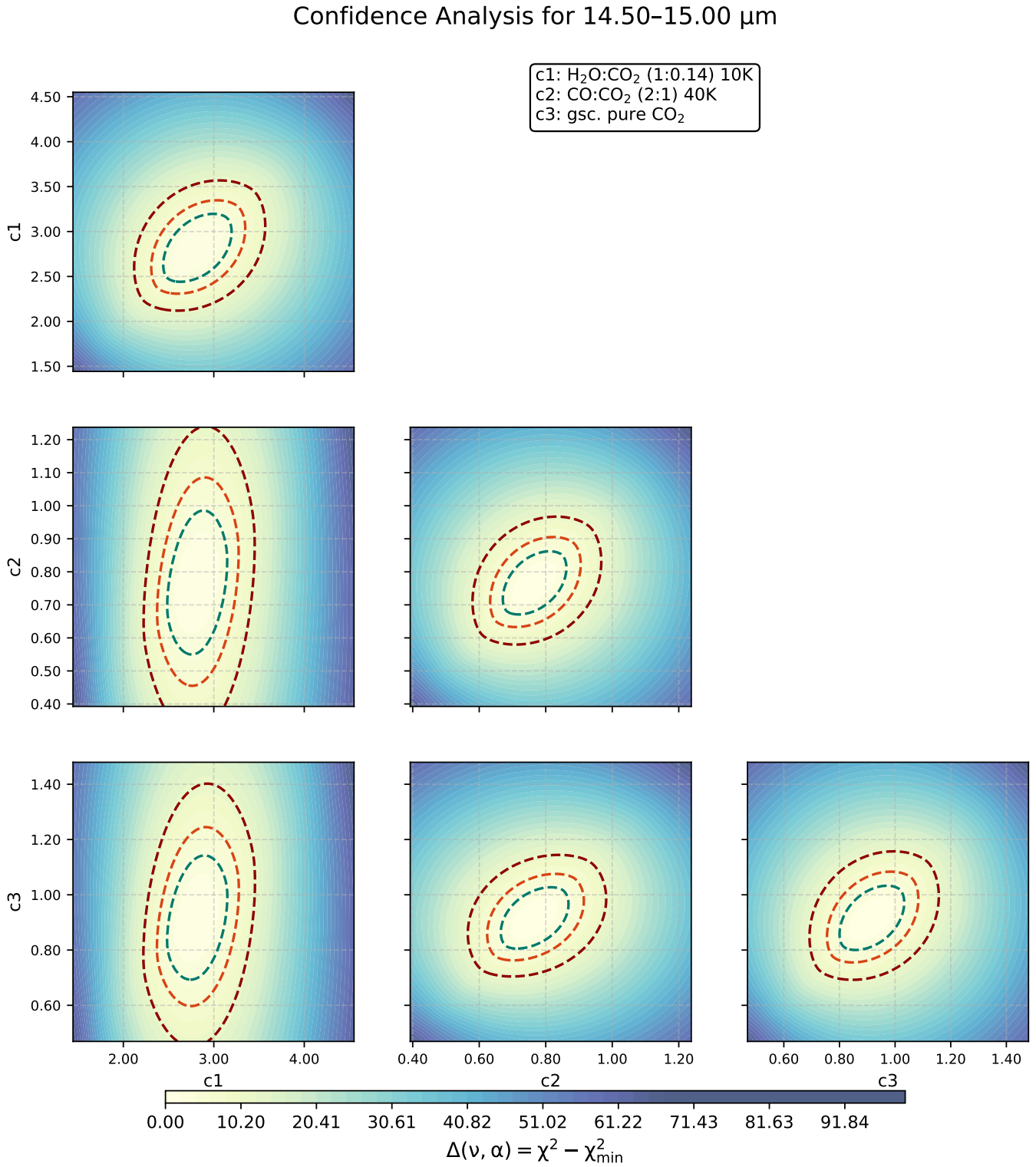

Figure 19. Confidence interval analysis of the CO_2 components based on χ^2 in the 14.50–15 μm region. The blue, red, and brown dotted lines indicate the 1σ, 2σ, and 3σ levels. The coefficients of the remaining components are kept constant while performing this analysis.

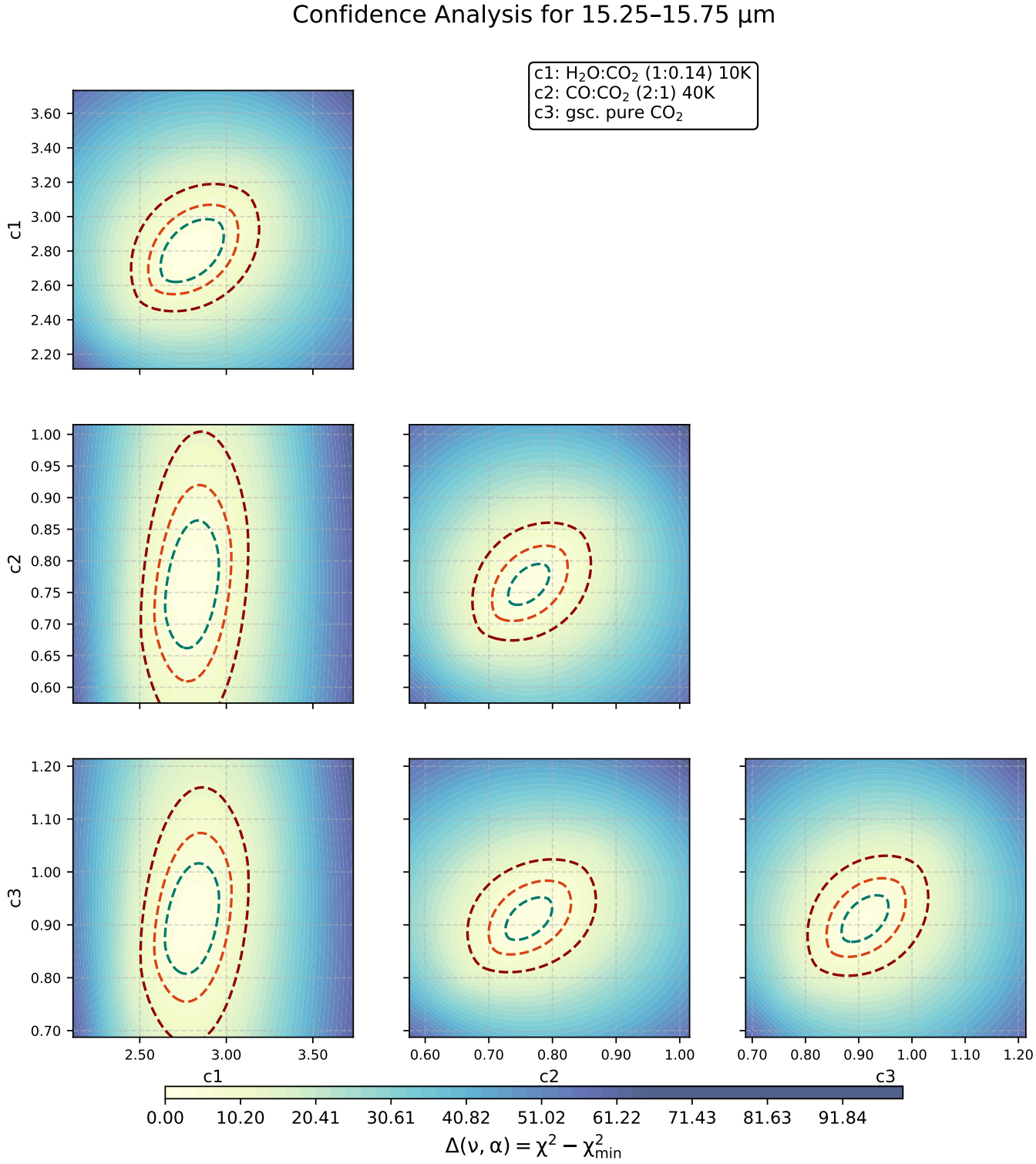

Figure 20. Confidence interval analysis of the CO_2 components based on χ^2 in the 15.25–15.75 μm region. The blue, red, and brown dotted lines indicate the 1σ, 2σ, and 3σ levels. The coefficients of the remaining components are kept constant while performing this analysis.

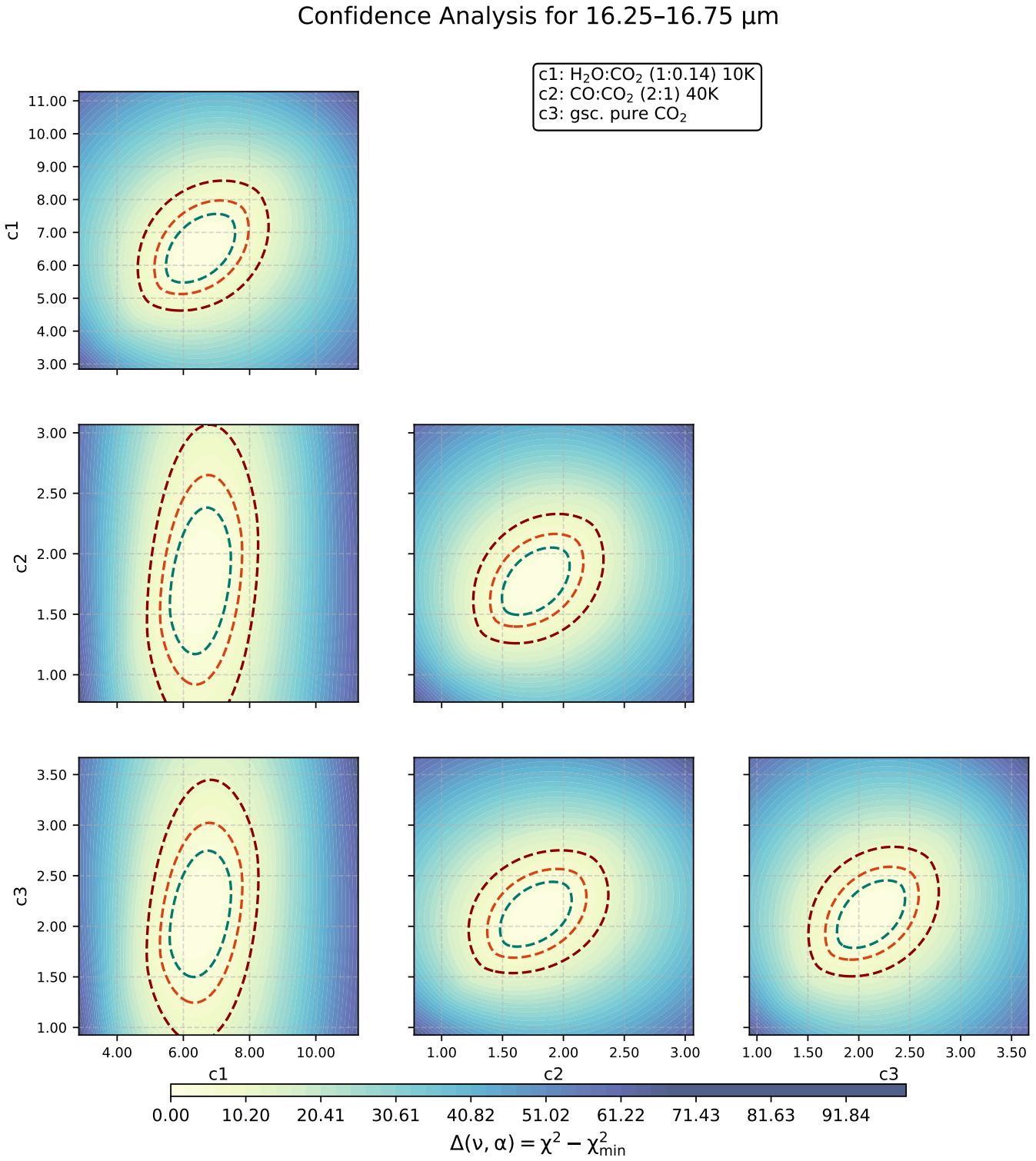

Figure 21. Confidence interval analysis of the CO_2 components based on χ^2 in the 16.25–16.75 μm region. The blue, red, and brown dotted lines indicate the 1σ, 2σ, and 3σ levels. The coefficients of the remaining components are kept constant while performing this analysis.

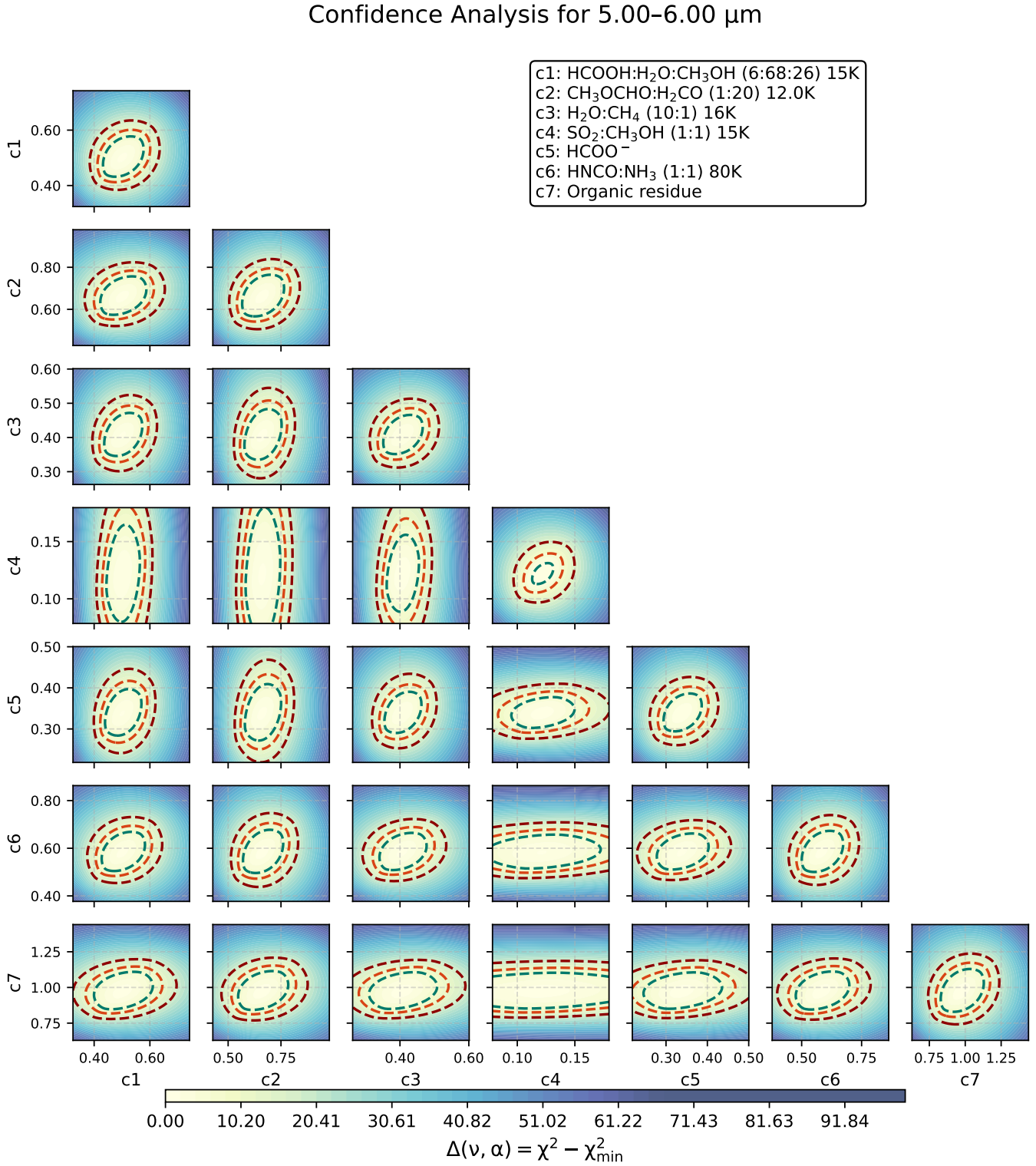

Figure 22. Confidence interval analysis of the components without H_2O and CO_2 bands based on χ^2 contributing in the 5–6 μm region. The blue, red, and brown dotted lines indicate the 1σ, 2σ, and 3σ levels. The coefficients of the remaining components are kept constant while performing this analysis.

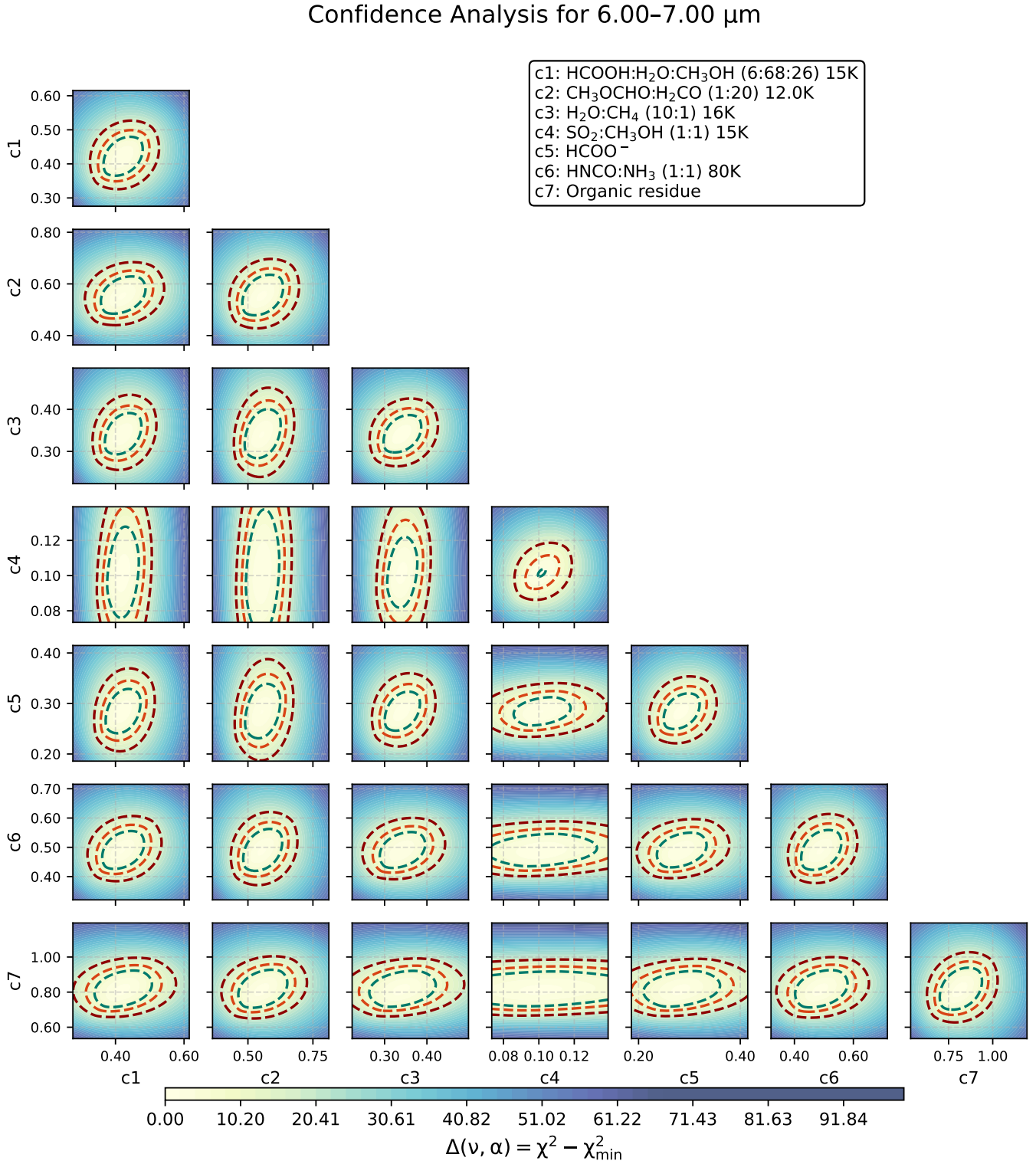

Figure 23. Confidence interval analysis of the components without H_2O and CO_2 bands based on χ^2 that are contributing in the 14.5–17.5 μm region. The blue, red, and brown dotted lines indicate the 1σ, 2σ, and 3σ levels. The coefficients of the remaining components are kept constant while performing this analysis.

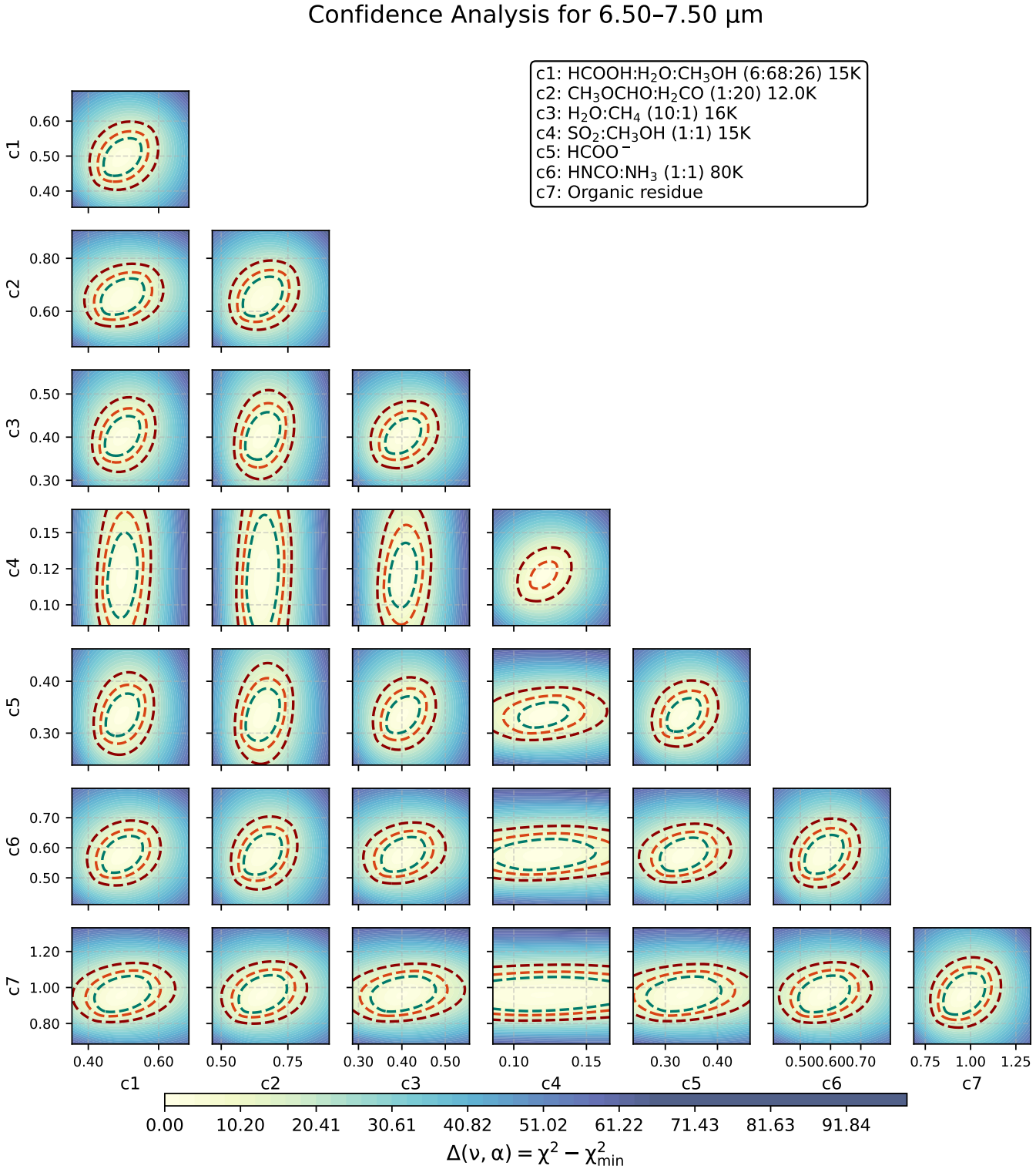

Figure 24. Confidence interval analysis of the components without H_2O and CO_2 bands based on χ^2 in the 5–11 μm region. The blue, red, and brown dotted lines indicate the 1σ, 2σ, and 3σ levels. The coefficients of the remaining components are kept constant while performing this analysis.

ORCID iDs

Prathap Rayalacheruvu https://orcid.org/0009-0001-6483-7366
Liton Majumdar https://orcid.org/0000-0001-7031-8039
W. R. M. Rocha https://orcid.org/0000-0001-6144-4113
Michael E. Ressler https://orcid.org/0000-0001-5644-8830
Pabitra Ranjan Giri https://orcid.org/0009-0008-6173-2519
S. Maitrey https://orcid.org/0000-0003-3412-9454
Karen Willacy https://orcid.org/0000-0001-6124-5974
D. C. Lis https://orcid.org/0000-0002-0500-4700
Yuan Chen https://orcid.org/0000-0002-3395-5634
P. D. Klaassen https://orcid.org/0000-0001-9443-0463

References

Ahmad, A., Misra, A., Tandon, P., et al. 2020, RAA, 20, 014
Argyriou, I., Glasse, A., Law, D. R., et al. 2023, A&A, 675, A111
Belloche, A., Maury, A. J., Maret, S., et al. 2020, A&A, 635, A198
Bennett, C. J., & Kaiser, R. I. 2007, ApJ, 660, 1289
Bergantini, A., Zhu, C., & Kaiser, R. I. 2018, ApJ, 862, 140
Bisschop, S. E., Fuchs, G. W., Boogert, A. C. A., van Dishoeck, E. F., & Linnartz, H. 2007, A&A, 470, 749
Boogert, A. C. A., Brewer, K., Brittain, A., & Emerson, K. S. 2022, ApJ, 941, 32
Boogert, A. C. A., Gerakines, P. A., & Whittet, D. C. B. 2015, ARA&A, 53, 541
Boogert, A. C. A., Schutte, W. A., Helmich, F. P., Tielens, A. G. G. M., & Wooden, D. H. 1997, A&A, 317, 929
Boogert, A. C. A., Pontoppidan, K. M., Knez, C., et al. 2008, ApJ, 678, 985
Bottinelli, S., Boogert, A. C. A., Bouwman, J., et al. 2010, ApJ, 718, 1100
Bottinelli, S., Ceccarelli, C., Williams, J. P., & Lefloch, B. 2007, A&A, 463, 601
Boudin, N., Schutte, W. A., & Greenberg, J. M. 1998, A&A, 331, 749
Bouilloud, M., Fray, N., Bénilan, Y., et al. 2015, MNRAS, 451, 2145
Bouwman, J., Ludwig, W., Awad, Z., et al. 2007, A&A, 476, 995
Brunken, N. G. C., Boogert, A. C. A., van Dishoeck, E. F., et al. 2025, ESC, 9, 1992
Brunken, N. G. C., van Dishoeck, E. F., Slavicinska, K., et al. 2024, A&A, 692, A163
Bushouse, H., Eisenhamer, J., Dencheva, N., et al. 2022, spacetelescope/jwst: JWST 1.6.2, v1.6.2, Zenodo, doi:10.5281/zenodo.6984366
Carrasco-Herrera, R., Bouquet, A., Danger, G. Â., et al. 2024, Europlanet Science Congress 2024, EPSC2024–367
Caselli, P., Walmsley, C., Tafalla, M., Dore, L., & Myers, P. 1999, ApJ, 523, L165
Chen, Y., Rocha, W. R. M., van Dishoeck, E. F., et al. 2024, A&A, 690, A205
Chen, Y., van Gelder, M. L., Nazari, P., et al. 2023, A&A, 678, A137
Chu, L. E. U., Hodapp, K., & Boogert, A. 2020, ApJ, 904, 86
Chuang, K. J., Fedoseev, G., Ioppolo, S., van Dishoeck, E. F., & Linnartz, H. 2016, MNRAS, 455, 1702
Chuang, K.-J., Fedoseev, G., Qasim, D., et al. 2017, MNRAS, 467, 2552
Chuang, K. J., Fedoseev, G., Qasim, D., et al. 2020, A&A, 635, A199
Coutens, A., Persson, M. V., Jørgensen, J. K., Wampfler, S. F., & Lykke, J. M. 2015, A&A, 576, A5
Danger, G., Honold, L., Ruf, A., et al. 2024, Europlanet Science Congress 2024, EPSC2024–596
Dartois, E. 2006, A&A, 445, 959
Dartois, E., Noble, J. A., Ysard, N., Demyk, K., & Chabot, M. 2022, A&A, 666, A153
Dartois, E., Schutte, W., Geballe, T. R., et al. 1999, A&A, 342, L32
Dartois, E., Thi, W. F., Geballe, T. R., et al. 2003, A&A, 399, 1009
De Simone, M., Codella, C., Testi, L., et al. 2017, A&A, 599, A121
Dominik, C., Min, M., & Tazaki, R., 2021 OpTool: Command-line Driven Tool for Creating Complex Dust Opacities, Astrophysics Source Code Library, ascl:2104.010
Ehrenfreund, P., Boogert, A. C. A., Gerakines, P. A., et al. 1996, A&A, 315, L341
Ehrenfreund, P., Boogert, A. C. A., Gerakines, P. A., Tielens, A. G. G. M., & van Dishoeck, E. F. 1997, A&A, 328, 649
Ehrenfreund, P., & Charnley, S. B. 2000, ARA&A, 38, 427
Fedoseev, G., Ioppolo, S., Zhao, D., Lamberts, T., & Linnartz, H. 2014, MNRAS, 446, 439
Fedoseev, G., Qasim, D., Chuang, K.-J., et al. 2022, ApJ, 924, 110
Fuchs, G. W., Cuppen, H. M., Ioppolo, S., et al. 2009, A&A, 505, 629
Gálvez, O., Maté, B., Herrero, V. J., & Escribano, R. 2010, ApJ, 724, 539
Garrod, R. T., & Herbst, E. 2006, A&A, 457, 927
Garrod, R. T., Jin, M., Matis, K. A., et al. 2022, ApJS, 259, 1
Gerakines, P., Schutte, W., & Ehrenfreund, P. 1996, A&A, 312, 289
Gerakines, P. A., Materese, C. K., & Hudson, R. L. 2025, MNRAS, 537, 2918
Gerakines, P. A., Schutte, W. A., Greenberg, J. M., & van Dishoeck, E. F. 1995, A&A, 296, 810
Gibb, E. L., & Whittet, D. C. B. 2002, ApJL, 566, L113
Gibb, E. L., Whittet, D. C. B., Boogert, A. C. A., & Tielens, A. G. G. M. 2004, ApJS, 151, 35
Gibb, E. L., Whittet, D. C. B., & Chiar, J. E. 2001, ApJ, 558, 702
Gieser, C., Beuther, H., Semenov, D., et al. 2021, A&A, 648, A66
Glassgold, A. E., Meijerink, R., & Najita, J. R. 2009, ApJ, 701, 142
Greenfield, P., & Miller, T. 2016, A&C, 16, 41
Grim, R. J. A., Baas, F., Geballe, T. R., Greenberg, J. M., & Schutte, W. A. 1991, A&A, 243, 473
Grim, R. J. A., & Greenberg, J. M. 1987, ApJL, 321, L91
Hänni, N., Altwegg, K., Combi, M., et al. 2022, NatCo, 13, 3639
Hasegawa, T. I., & Herbst, E. 1993, MNRAS, 261, 83
He, Y. Y., Bernard, S., Lecasble, M., et al. 2024, GeCoA, 387, 98
Herbst, E., & Klemperer, W. 1973, ApJ, 185, 505
Hidaka, H., Watanabe, M., Kouchi, A., & Watanabe, N. 2011, PCCP, 13, 15798
Hiraoka, K., Yamashita, A., Yachi, Y., et al. 1995, ApJ, 443, 363
Hudgins, D. M., Sandford, S. A., Allamandola, L. J., & Tielens, A. G. G. M. 1993, ApJS, 86, 713
Hudson, R. L., & Ferrante, R. F. 2020, MNRAS, 492, 283
Hudson, R. L., Moore, M. H., & Cook, A. M. 2005, AdSpR, 36, 184
Hudson, R. L., Moore, M. H., & Gerakines, P. A. 2001, ApJ, 550, 1140
Huntress, W., Jr., & Mitchell, G. 1979, ApJ, 231, 456
Ishii, M., Nagata, T., Chrysostomou, A., & Hough, J. H. 2002, AJ, 124, 2790
Javelle, T., Ruf, A., Bouquet, A., Schmitt-Kopplin, P., & Danger, G. 2024, MNRAS, 534, 2305
Jiménez-Serra, I., Megías, A., Salaris, J., et al. 2025, A&A, 695, A247
Jin, M., Remijan, A. J., Garrod, R. T., et al. 2025, ApJ, 987, 100
Jørgensen, J. K., Belloche, A., & Garrod, R. T. 2020, ARA&A, 58, 727
Kleimeier, N. F., Eckhardt, A. K., & Kaiser, R. I. 2020, ApJ, 901, 84
Labiano, A., Argyriou, I., Álvarez-Márquez, J., et al. 2021, A&A, 656, A57
Lamberts, T., Fedoseev, G., van Hemert, M. C., et al. 2022, ApJ, 928, 48
Looney, L. W., Mundy, L. G., & Welch, W. J. 2000, ApJ, 529, 477
Luna, R., Molpeceres, G., Ortigoso, J., et al. 2018, A&A, 617, A116
Luo, J., Ying, K., & Bai, J. 2005, SigPr, 85, 1429
Manigand, S., Jørgensen, J. K., Calcutt, H., et al. 2020, A&A, 635, A48
Mathurin, J., Bejach, L., Dartois, E., et al. 2024, A&A, 684, A198
McClure, M. K., Rocha, W. R. M., Pontoppidan, K. M., et al. 2023, NatAs, 7, 431
Mehringer, D. M., Snyder, L. E., Miao, Y., & Lovas, F. J. 1997, ApJ, 480, L71
Molpeceres, G., Nguyen, T., Oba, Y., & Watanabe, N. 2025, A&A, 694, A299
Molpeceres, G., Rimola, A., Ceccarelli, C., et al. 2018, MNRAS, 482, 5389
Muñoz Caro, G. M., & Schutte, W. A. 2003, A&A, 412, 121
Nazari, P., van Gelder, M. L., van Dishoeck, E. F., et al. 2021, A&A, 650, A150
Novozamsky, J. H., Schutte, W. A., & Keane, J. V. 2001, A&A, 379, 588
Oba, Y., Takano, Y., Naraoka, H., et al. 2020, NatCo, 11, 6243
Öberg, K. I., & Bergin, E. A. 2021, PhR, 893, 1
Öberg, K. I., Boogert, A. C. A., Pontoppidan, K. M., et al. 2008, ApJ, 678, 1032
Öberg, K. I., Boogert, A. C. A., Pontoppidan, K. M., et al. 2011, ApJ, 740, 109
Öberg, K. I., Fraser, H. J., Boogert, A. C. A., et al. 2007, A&A, 462, 1187
Pontoppidan, K. M., Boogert, A. C. A., Fraser, H. J., et al. 2008, ApJ, 678, 1005
Pontoppidan, K. M., Dullemond, C. P., van Dishoeck, E. F., et al. 2005, ApJ, 622, 463
Pontoppidan, K. M., van Dishoeck, E. F., & Dartois, E. 2004, A&A, 426, 925
Qasim, D., Fedoseev, G., Chuang, K.-J., et al. 2020, NatAs, 4, 781
Rachid, M. G., Brunken, N., de Boe, D., et al. 2021, A&A, 653, A116
Rachid, M. G., Rocha, W. R. M., & Linnartz, H. 2022, A&A, 665, A89
Rachid, M. G., Terwisscha van Scheltinga, J., Koletzki, D., & Linnartz, H. 2020, A&A, 639, A4
Reipurth, B., Rodríguez, L. F., Anglada, G., & Bally, J. 2002, AJ, 124, 1045
Remijan, A., Snyder, L., Liu, S.-Y., Mehringer, D., & Kuan, Y.-J. 2002, ApJ, 576, 264
Rieke, G. H., Wright, G. S., Böker, T., et al. 2015, PASP, 127, 584
Rocha, W. R. M., Perotti, G., Kristensen, L. E., & Jørgensen, J. K. 2021, A&A, 654, A158

Rocha, W. R. M., Pilling, S., de Barros, A. L. F., et al. 2017, MNRAS, 464, 754
Rocha, W. R. M., Pilling, S., Domaracka, A., Rothard, H., & Boduch, P. 2020, AcSpA, 228, 117826
Rocha, W. R. M., van Dishoeck, E. F., Ressler, M. E., et al. 2024, A&A, 683, A124
Rocha, W. R. M., McClure, M. K., Sturm, J. A., et al. 2025, A&A, 693, A288
Rubin, M., Altwegg, K., Balsiger, H., et al. 2019, MNRAS, 489, 594
Sandell, G., Knee, L. B. G., Aspin, C., Robson, I. E., & Russell, A. P. G. 1994, A&A, 285, L1
Savitzky, A., & Golay, M. J. E. 1964, AnaCh, 36, 1627
Schutte, W. A., Boogert, A. C. A., Tielens, A. G. G. M., et al. 1999, A&A, 343, 966
Schutte, W. A., & Khanna, R. K. 2003, A&A, 398, 1049
Scott, G. B. I., Fairley, D. A., Freeman, C. G., & McEwan, M. J. 1997, CPL, 269, 88
Shimonishi, T., Onaka, T., Kato, D., et al. 2010, A&A, 514, A12
Sivaramakrishnan, R., Michael, J. V., & Klippenstein, S. J. 2010, JPCA, 114, 755
Skinner, C. J., Tielens, A. G. G. M., Barlow, M. J., & Justtanont, K. 1992, ApJL, 399, L79
Slavicinska, K., Boogert, A. C. A., Tychoniec, Ł., et al. 2025, A&A, 693, A146
Slavicinska, K., Rachid, M. G., Rocha, W. R. M., et al. 2023, A&A, 677, A13
Taquet, V., López-Sepulcre, A., Ceccarelli, C., et al. 2015, ApJ, 804, 81
Terwisscha van Scheltinga, J., Ligterink, N. F. W., Boogert, A. C. A., van Dishoeck, E. F., & Linnartz, H. 2018, A&A, 611, A35
Terwisscha van Scheltinga, J., Marcandalli, G., McClure, M. K., Hogerheijde, M. R., & Linnartz, H. 2021, A&A, 651, A95
Thi, W. F., van Dishoeck, E. F., Dartois, E., et al. 2006, A&A, 449, 251
Tobin, J. J., Dunham, M. M., Looney, L. W., et al. 2015, ApJ, 798, 61
Urso, R. G., Alemanno, G., Baratta, G. A., et al. 2024, Europlanet Science Congress 2024, EPSC2024–800
Van Broekhuizen, F. A., Keane, J. V., & Schutte, W. A. 2004, A&A, 415, 425
Van Broekhuizen, F. A., Pontoppidan, K. M., Fraser, H. J., & van Dishoeck, E. F. 2005, A&A, 441, 249
van Gelder, M. L., Ressler, M. E., van Dishoeck, E. F., et al. 2024, A&A, 682, A78
van Gelder, M. L., Tabone, B., Tychoniec, Ł., et al. 2020, A&A, 639, A87
Wagner, E. L., & Hornig, D. F. 1950, JChPh, 18, 296
Watanabe, N., & Kouchi, A. 2002, ApJL, 571, L173
Weingartner, J. C., & Draine, B. T. 2001, ApJ, 548, 296
Wells, M., Pel, J. W., Glasse, A., et al. 2015, PASP, 127, 646
Woitke, P., Min, M., Pinte, C., et al. 2016, A&A, 586, A103
Wright, G. S., Rieke, G. H., Glasse, A., et al. 2023, PASP, 135, 048003
Wright, G. S., Wright, D., Goodson, G. B., et al. 2015, PASP, 127, 595
Yang, Y.-L., Green, J. D., Pontoppidan, K. M., et al. 2022, ApJL, 941, L13